Permo-Carboniferous and early Miocene geological evolution of the internal zones of the Maghrebides - New insights on the western Mediterranean evolution

Laure Fernandez, Delphine Bosch, Olivier Bruguier, Dalila Hammor, Renaud Caby, Patrick Monie, Nicolas Olivier Arnaud, Abder Toubal, Beatrice Galland, Chantal Douchet

Permo-Carboniferous and early Miocene geological evolution of the internal zones of the Maghrebides – New insights on the western Mediterranean evolution

Laure Fernandez[a,*], Delphine Bosch[a], Olivier Bruguier[a], Dalila Hammor[b], Renaud Caby[a], Patrick Monié[a], Nicolas Arnaud[a], Abder Toubal[b], Béatrice Galland[a], Chantal Douchet[a]

[a] *Géosciences Montpellier, UMR CNRS 5243, Université de Montpellier, Place E. Bataillon, 34 095 Montpellier cedex 5, France*
[b] *Laboratoire de Recherche de Géologie, Faculté des Sciences de la Terre, Université Badji-Mokhtar, BP 12, Annaba 23 000, Algeria*

Keywords:
Geochemistry
Geochronology
Western Mediterranean
Maghrebides
Miocene
Permo-Carboniferous

a b s t r a c t

Geochemical and geochronological analyses were performed on metamorphic rocks from the footwall of an oceanic unit thrusted onto the North African margin. The footwall is mainly constituted by metamorphosed sediments and interlayered mafic rocks with scarce ultramafic lenses. Major and trace elements geochemistry of the sediments is consistent with a passive margin setting ($16.9 < K_2O/Na_2O < 20.9$; $18.2 < Zr/Th < 24.6$). U–Pb analyses of detrital zircons indicate that deposition of the sedimentary sequence is younger than 307 ± 7 Ma (2) and concur with a provenance of the detritus from the Eastern Meseta and High Atlas of Morocco. The age of a crosscutting orthogneiss (281 ± 4 Ma) further constrains deposition to the upper Carboniferous/lower Permian times (307–281 Ma), in good agreement with the 295 ± 2 Ma age of an interbedded amphibolite. Geochemistry of the mafic and ultramafic rocks displays subduction related features (LILE and LREE enrichments, HFSE depletion). Pb, Sr, Nd and Hf isotopes further indicate a depleted mantle reservoir modified by a continental crust-derived component brought into the mantle during an ancient subduction event. The range of isotopic compositions and geochemical signatures displayed by the Carboniferous mafic rocks suggest they inherited their geochemical characteristics during melting of a heterogeneous lithospheric mantle containing variable metasomatic additions. Geochronological results indicate that the HT metamorphic evolution of this upper Paleozoic sequence resulted from two distinct events, each followed by fast cooling. The first one, dated at 20.85 ± 0.34 Ma (2), followed HP metamorphism and thrusting of the Kef Lakhal oceanic complex onto the Northern margin of Africa. The second event occurred at 17.65 ± 0.46 Ma (2) and is coeval with exhumation and anatexis of the lower crustal units of the neighbouring Edough dome. Fast cooling of the footwall rocks, through the closure temperatures of muscovite and biotite, occurred synchronously at 16.94 ± 0.10 Ma (2) and 17.02 ± 0.19 Ma (2) respectively. This study documents a further example of the complex history recorded by rocks of the Peri-Mediterranean area that contains an imbrication of geological units, witnesses of a protracted history related to Permo-Carboniferous and Miocene events.

1. Introduction

The western Mediterranean basin is wrapped by an alpine peri-Mediterranean mountain belt that runs from the Betics in Spain to NE Tunisia through the Rif and the Tell in Morocco and Algeria (Fig. 1a). Key features include the occurrence of mantle material emplaced into continental crustal units (including the Ronda Massif, the world's largest outcrop of subcontinental mantle, Obata, 1980) and diamond-bearing units, either of continental (e.g. Ruiz-Cruz and De Galdeano, 2012) or of mantle origin (Caby et al., 2014). Mantle materials constitute important elements in order to reconstruct the architecture as well as the tectonic evolution of the orogens (e.g. Zindler et al., 1983; Blichert-Toft et al., 1999). As a consequence, numerous studies have thus largely focused on these materials, whereas the high-grade metamorphic rocks, often polymetamorphosed, constituting the footwall of the allochtonous mantle rocks have often been forsaken. The study of these rocks is however a major issue as it may provide insights contributing to a better understanding of the processes that take place when the mantle fragments are emplaced onto the continental margins (e.g.

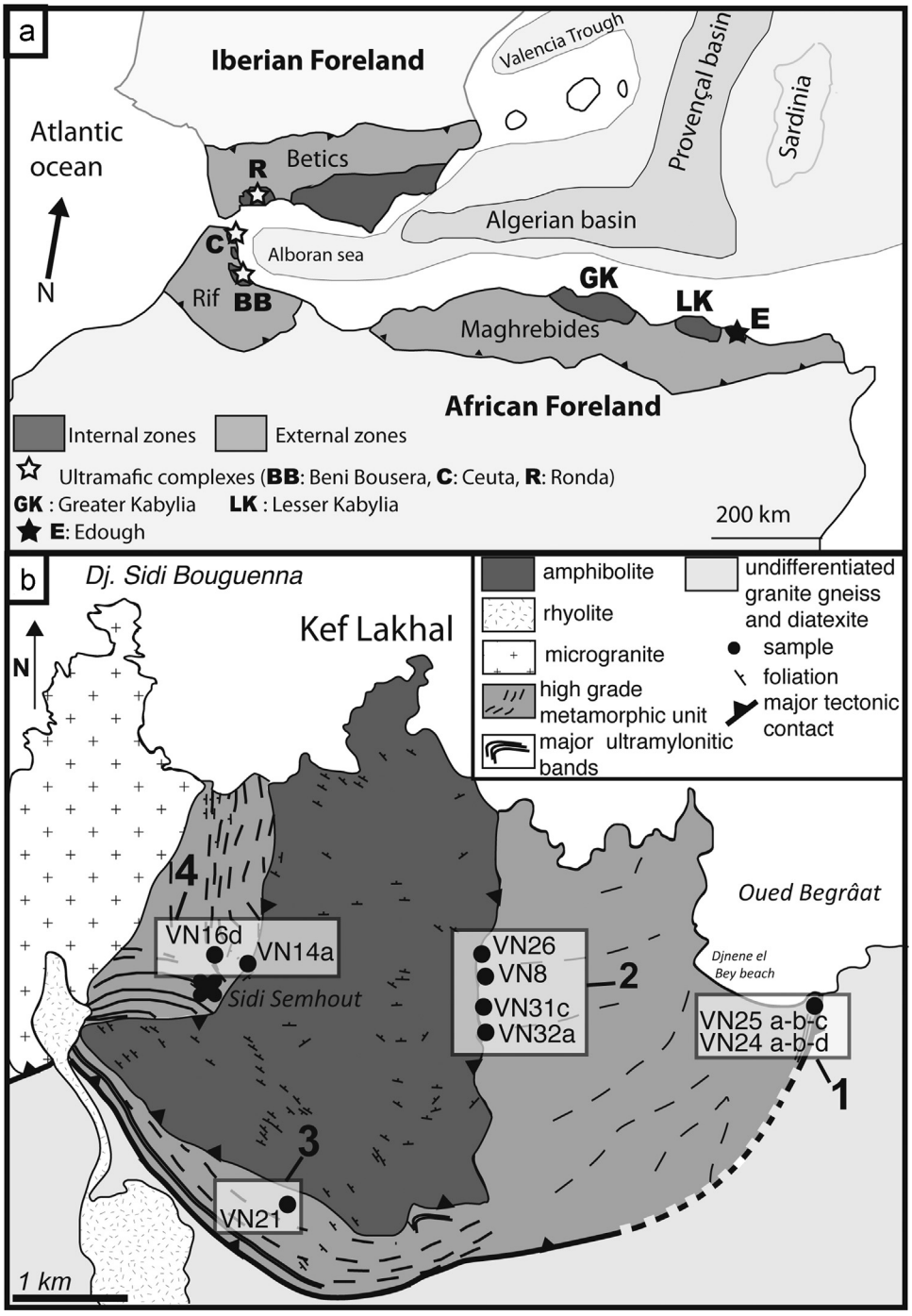

Fig. 1. (a) Tectonic sketch map of the Western Mediterranean basin showing the location of the Maghrebides within the framework of the west Mediterranean orogen (modified after Frizon de Lamotte et al., 2000). (b) Geological sketch map of the Kef Lakhal area in the Edough massif of NE Algeria (modified from Caby et al., 2014). Reported foliations are from Ahmed-Said and Leake, 1992). Squares 1–4 refer to localities mentioned in the text.

Rossetti et al., 2010; Romagny et al., 2014). In addition, the nature and geotectonic setting of these units as well as the age of metamorphism that affected them during emplacement of the mantle rocks, are potentially accessible for paleogeodynamical reconstructions (e.g. Frizon de Lamotte et al., 1991; Royden, 1993; Lonergan and Platt, 1995; Lonergan and White, 1997; Faccenna et al., 2001; Jolivet et al., 2008).

In this contribution, we focused on the high-grade metamorphic rocks outcropping in the northwestern part of the Edough Massif of NE Algeria at the northern limit of the Edough dome (Fig. 1b). These rocks were overthrust by the Kef Lakhal amphibolite complex of oceanic origin (Ahmed-Said and Leake, 1992, 1997; Bosch et al., 2014) and thrust over the edge of the African margin, probably during the incipient opening of the Algerian basin (Caby et al., 2001). The main aim of the study is to characterize the nature and paleogeodynamic environment of the high-grade rocks from the footwall unit, to determine whether they are allochtonous or (para)autochtonous in origin and to constrain the age of metamorphism that affected them. To reach this goal requires an integrated geochemical (major and trace elements, and Sr–Nd–Pb–Hf isotopes

on whole-rocks and separated minerals) and geochronological study (U–Pb, Sm–Nd and Ar–Ar) on samples collected at different levels of the footwall.

2. Geodynamical and geological setting

The Edough massif, in northeastern Algeria, is part of the Maghrebides mountain belt, a collisional zone extending from Morocco to Algeria, which represents the southern segment of the Peri-Mediterranean Alpine belt (Fig. 1a). The Maghrebides resulted from the Cenozoic fragmentation of the European paleomargin and the drifting of the resulting fragments, the so-called Alkapeca terrane of Bouillin (1986), some of which (such as the Lesser and Greater Kabylia) ultimately collided with the northern margin of Africa. Since the Cretaceous/Eocene, the paleogeodynamic evolution of the West Mediterranean can broadly be summarized as resulting from subduction processes affecting the Tethys Ocean beneath the continental European paleomargin. The initiation of the subduction is still debated and could have started as early as *c.* 80 Ma with a very slow convergence velocity between 80 and 35 Ma (Faccenna et al., 2001) or later, between *c.* 65 and 30 Ma (Dercourt et al., 1986; Doglioni et al., 1997; Carminati et al., 1998). Back-arc extension due to slab retreat began around 30 Ma (Augier et al., 2005; Jolivet et al., 2008) causing the opening of the Liguro-Provenc¸al basin and the rotation of the Corsica-Sardinia block (Advokaat et al., 2014). The opening of the Algerian basin, south of the Liguro-Provenc¸al basin is assumed to have occurred later, during the early Miocene (e.g. Carminati et al., 1998; Medaouri et al., 2014).

The Edough massif (Fig. 1b) displays a 40 km long structural dome shape oriented NE–SW that has been interpreted as a Miocene metamorphic core complex (Hammor, 1992; Caby and Hammor, 1992; Caby et al., 2001). The core of the massif is made up of granitoid, gneiss and migmatite associated with high-grade metasediments that are structurally overlain by pelitic schists of assumed Paleozoic age (Ilavsky and Snopkova, 1987) and on top, by outliers of Tellian Mesozoic metasediments caped by the Numidian flysch nappe. Previous geochronological studies on rocks from the massif have identified two main events at *c.* 17–20 and 280–310 Ma (Monié et al., 1992; Bruguier et al., 2009). The oldest range of ages was attributed to late Carboniferous magmatism overprinted by a Permian metamorphic event and were taken as emphasizing the polycyclic evolution of basement rocks preserved in the crystalline dome of the Edough massif (Bruguier et al., 2009). A small peridotite body, the Sidi Mohamed peridotites, first identified by Bossière et al. (1976), outcrops in the northeastern part of the dome and represents a piece of sub-continental mantle (Hadj-Zobir and Oberhänsli, 2013; Bosch et al., 2014) emplaced into the crustal units at 18 Ma (Bruguier et al., 2009). In the northwestern part of the massif, high-grade metamorphic units are present above the core units and include kyanite–sillimanite–andalusite-bearing sediments, marbles, diatexite and amphibolite lenses (Ahmed-Said and Leake, 1992, 1997). Southeast of the Kef Lakhal unit, some metasediments show two superimposed metamorphic events one of which is characterized by HT-HP metamorphic conditions (700–750 °C and 12–14 kbar after Caby et al., 2001). These high-grade rocks constitute the footwall of the Kef Lakhal amphibolite complex. Stable isotopes (O, S) on these amphibolites indicate that the magmas were contaminated by fluids originating from a sedimentary component (Laouar et al., 2002). The main mylonite zone that delineates oceanic units of the Kef Lakhal complex from high-grade metamorphic units below contains relics of UHP, diamond-bearing metamorphic rocks accreted to the base of the overriding Kef Lakhal complex during its thrusting over the African continental margin (Caby et al., 2014). Previous Ar–Ar ages performed by Monié et al. (1992) on high-grade metamorphic rocks from the Edough dome and Cap de Garde area range from 17.3±0.2 to 15.5±0.2 Ma for amphibole, muscovite and biotite. These ages were assigned to the late stages of extensional tectonics linked to exhumation of the core of the Edough dome. Besides, one orthogneiss from the Edough massif yielded a poorly constrained Sm–Nd isochron (whole-rock–garnet–feldspar) age of 25.4±10 Ma attributed to metamorphism in the dome (Hammor, 1992).

In the following sections we present petro-geochemical and geochronological constraints on metamorphosed sediments and igneous rocks located in the footwall of the Kef Lakhal amphibolite complex, which have been until now only scarcely investigated.

3. Analytical techniques

3.1. Major and trace elements

Rocks samples were crushed and then pulverized in an agate mill for whole-rock analyses (WR). Analyses of major elements on WR were performed at the "Service d'Analyse des Roches et des Minéraux" (SARM, Nancy, France) by X-ray fluorescence (XRF). Trace elements on WR were analysed by ICP-MS using an Agilent 7700 × from the "Analyse des Elements Trace dans l'Environnement (AETE)" technical plateform from Montpellier University (France). In situ major element analyses of minerals were performed at Montpellier University using an electron microprobe CAMECA SX100 with an accelerating voltage and beam current of 20 kV and 10 nA respectively and a counting time of 20–30 s. In situ trace element analyses of minerals were carried out by LA-ICP-MS at the Géosciences Montpellier laboratory using a ThermoFinnigan Element XR ICP-MS, coupled with a Geolas (Microlas) automated platform housing a 193 nm Compex 102 laser from LambdaPhysik. Signals were acquired in Time Resolved Acquisition mode, devoting 2 min for the blank and 1 min for measurement of the analytes. The laser was fired using an energy density of 15 J/cm^2 at a frequency of 5 Hz and using a spot size of 50–120 mm. Oxide level, measured by the ThO/Th ratio, was below 0.8%. Reference sample BIR-1G was analysed as an unknown during the analytical runs and shows good agreement with working values (Gao et al., 2002). Si was used as an internal standard and analyte concentrations were calibrated against the NIST 612 rhyolitic glass, according to the values of Pearce et al. (1997). Data were subsequently reduced using the GLITTER software (Van Achterberg et al., 2001) by inspecting the time-resolved spectra to check for heterogeneities in the analysed volume.

3.2. Isotopes

Sr–Nd–Pb–Hf isotopic analyses were performed on HCl6N-acid leached whole-rocks and mineral fractions. Leached WR, feldspar and amphibole were dissolved on a hot plate with a mixture of 48% HF and 13 N HNO_3 (1:1) and few drops of $HClO_4$. Pb was separated using anionic resin and HBr and HCl acids as reagents. Three successive concentration/purification steps were necessary to separate Sr, Nd and Hf. The procedures used were modified from Pin et al. (1995) and Connelly et al. (2006). Sr isotopic ratios were measured by thermal ionization mass spectrometry using a Triton Finnigan Mat spectrometer at Labogis from the Nîmes University. Pb, Nd and Hf analyses were performed using a Nu 500 HR MC-ICP-MS at the "Service Commun National d'Analyse" from the Ecole Normale Supérieure (ENS, Lyon, France). Sr, Nd, Pb and Hf total procedural blanks were less than 30, 10, 30 and 20 pg, respectively. Mass dependent fractionations were corrected using a $^{86}Sr/^{88}Sr$ ratio of 0.1194, a $^{146}Nd/^{144}Nd$ ratio of 0.7219 and a $^{179}Hf/^{177}Hf$ ratio of 0.7325 for Sr, Nd and Hf analyses, respectively. Standards

were measured repeatedly during the course of this study and yielded average values of $^{87}Sr/^{86}Sr = 0.710243 \pm 10$ (2 , $n = 7$) for the NBS987 standard, $^{143}Nd/^{144}Nd = 0.5119632 \pm 1$ (2 , $n = 7$) for the "Rennes" in-house Nd standard (Chauvel and Blichert-Toft, 2001) and $^{176}Hf/^{177}Hf = 0.282160 \pm 10$ (2 ,) for the JMC475 Hf standard (Blichert-Toft et al., 1997). NBS981 Pb standards were analysed every two samples and yielded a reproducibility better than 60 ppm. All measured isotopic ratios were corrected for in situ decay using a Miocene age at 20 Ma according to the U–Pb and Sm–Nd ages obtained during the course of this study.

3.3. U–Pb geochronology

Zircons were separated following standard separation techniques (Bosch et al., 1996). Around 50 zircons from each sample were selected from the least magnetic concentrates in order to obtain an assortment of the best quality crystals. Zircons were then embedded in epoxy resin together with chips of the 91500 zircon standard (Wiedenbeck et al., 1995), and polished to expose their internal structures. The laser (Lambda Physik CompEx 102 excimer laser) used for U–Th–Pb analyses was coupled to an Element XR sector field ICP-MS. Analytical procedures are after Bosch et al. (2011), and are only briefly summarized below.

Laser spot sizes were fixed to 26 mm. Samples were ablated under ultrapure helium in a 15 cm^3, circular shaped cell with an energy density of 12 J/cm^2 at a frequency of 4 Hz. The helium gas stream was then mixed with argon before entering the plasma. The mean oxide value (ThO/Th) during analyses was <1%. Acquisition lasted 45 s and the blank was measured before each new analysis during 15 s. All isotopes (^{202}Hg, $^{204}Pb + Hg$, ^{206}Pb, ^{207}Pb, ^{208}Pb, ^{232}Th and ^{238}U) were measured in pulse counting mode. Unknowns were bracketed by analyses of the G91500 standard (Wiedenbeck et al., 1995), which were used to calculate a mass bias factor (Pb/Pb ratio) and the inter-element fractionation (U/Pb ratios). The calculated bias factors and associated errors were then added in quadrature to individual errors measured on each unknown (after Horstwood et al., 2003). The decay constants and present-day $^{238}U/^{235}U$ value given by Steiger and Jäger (1977) were used and ages were calculated using the program Isoplot/Ex of Ludwig (2002). Zircons showing a degree of discordance in the range 10% were classified as concordant within errors and weighted mean ages were calculated for batches of such concordant analyses.

3.4. Ar–Ar geochronology

Biotite, muscovite and amphibole were handpicked in the 80–150 mm fractions after magnetic separation using a Frantz magnetic separator. After ultrasonic cleaning in ultrapure acetone and distilled water, minerals were conditioned in aluminium foil packets and irradiated for 40 h in the TRIGA Mark-II reactor of Pavia University (Italy) with aliquots of the Fish Canyon sanidine standard (28.03 0.08 Ma; Jourdan and Renne, 2007) as flux monitor. Argon isotopic interferences on K and Ca were determined by irradiation of KF and CaF_2 pure salts from which the following correction factors were obtained: $(^{40}Ar/^{39}Ar)_K = 0.00969$ 0.00038, $(^{38}Ar/^{39}Ar)_K = 0.01297$ 0.00045, $(^{39}Ar/^{37}Ar)_{Ca} = 0.0007474$ 0.000021 and $(^{36}Ar/^{37}Ar)_{Ca} = 0.000288$ 0.000016. Argon analyses were performed at Géosciences Montpellier (France) with an analytical system that consists of: (a) an IR-CO_2 laser of 100 kHz used at 5–15% during 60 s, (b) a lenses system for beam focusing, (c) a steel chamber, maintained at 10^{-8}–10^{-9} bar, with a drilled copper plate and the four samples on, (d) an inlet line for purification of gases including two Zr–Al getters, (e) a multi-collector mass spectrometer (Argus VI from Thermo-Fisher). A custom-made software controls the laser intensity, the timing of extraction/purification and the data acquisition. To measure the argon background within the system, one blank analysis was performed every three sample analyses. The ArArCalc software© v2.5.2 was used for data reduction and plotting. The two-sigma errors reported on plateau, isochron and total gas ages include the error on the irradiation factor *J*. Atmospheric ^{40}Ar was estimated using a value of the initial $^{40}Ar/^{36}Ar$ of 295.5 (Steiger and Jäger, 1977). Data are portrayed as age spectra in Fig. 9a–i and summarized in Table 3. A complete set of isotopic results is given in Supplementary Appendix.

4. Results

4.1. Sample description

4.1.1. Field relationships

Four main areas were sampled in the high-grade metamorphic units constituting the footwall of the Kef Lakhal complex (localities 1–4 in Fig. 1b). These localities are broadly similar to those described in Caby et al. (2014).

At locality 1 (see Fig. 2) field relationships between the different lithologies can be clearly observed. A mylonite/ultramylonite

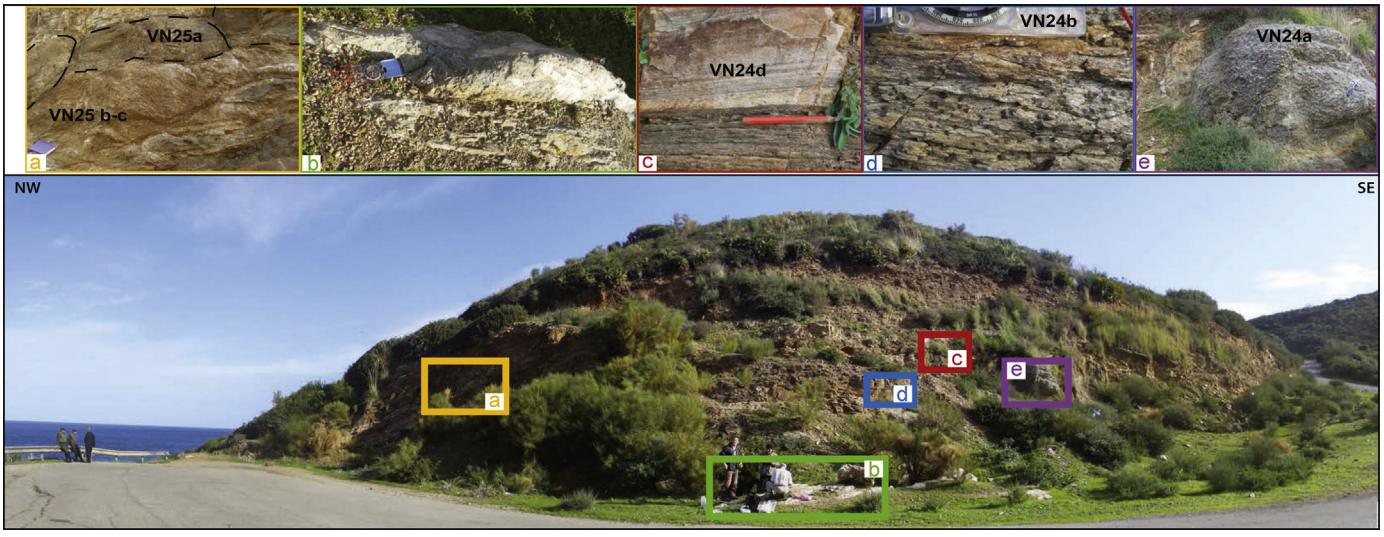

Fig. 2. Panoramic photograph of locality 1. Insets show the different lithologies: (a) amphibolite lens VN25a intercalated within micaschist VN25b; (b) wollastonite lenses; (c) orthogneiss VN24d; (d) micaschist VN24b displaying white mica and garnet; and (e) peridotite lens VN24a of 2 m in size.

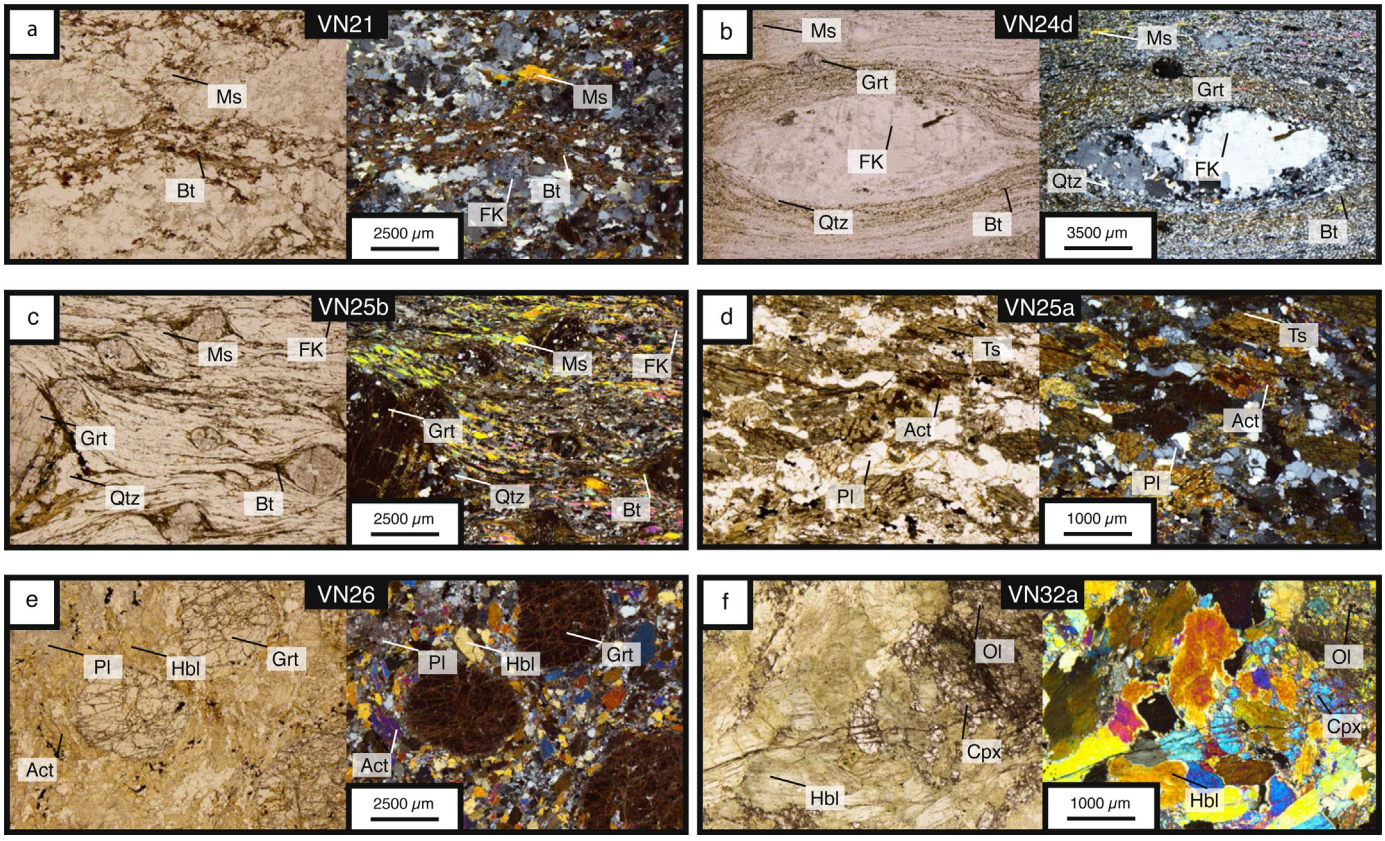

Fig. 3. Thin section microphotographs in plane and cross-polarized mode. (a) Diatexite VN21 showing muscovite, perthitic K-feldspar and primary biotite associated to secondary biotite + sillimanite (fibrolite) materialized by shiny aureoles around brown biotite. (b) Mylonitized orthogneiss (VN24d) presenting myrmekite next to K-feldspar phenocryst associated to small garnet containing primary mica inclusions. The photograph displays a finely grained matrix constituted of quartz, small muscovite mica-fishes and late biotite + sillimanite. (c) micaschist VN25b displaying garnet porphyroclasts with inclusion-rich cores. The occurrence of a biotite + sillimanite (fibrolite) assemblage in garnet tails points to garnet destabilization. (d) Slightly deformed amphibolite VN25a showing plagioclase and amphibole (tschermakite and actinote). (e) Garnet amphibolite VN26 showing strongly cataclased garnet associated to amphibole, quartz and plagioclase. (f) Ultramafic rock VN32a presenting secondary amphibole megacrysts associated with serpentinized olivine and small, rare primary clinopyroxene. Symbols after Kretz (1983).

band (*c*. 15 m thick) sharply delimits the high-grade rocks from the granite–gneiss rocks of the dome. Garnet micaschists (samples VN24b, VN25b and VN25c) contain decimeter-sized amphibolite lenses (VN25a) parallel to schistosity and a metre-sized boudin of coarse-grained peridotite (VN24a) surrounded by a brownish two metres wide alteration zone (Fig. 2a–e). Micaschists are locally intruded by a fine-grained orthogneiss (VN24d) oriented parallel to the main schistosity. Contact between the orthogneiss and metasediments is sharp and suggests intrusive relationship. In addition a small level of wollastonite marble was also observed within this rock association (Fig. 2b).

Samples collected at locality 2, close to the contact with the Kef Lakhal complex (Fig. 1b, samples VN8, VN26, VN31c, VN32a) are exposed through road cuts, often as lenses of limited size, but field relationships are unclear due to poor outcrop quality and deformation related to the vicinity of the main contact zone. By similarity with locality 1, it is proposed that the amphibolites represent sills interbedded in the metasediments.

Diatexite VN21 (locality 3 of Fig. 1b) is a partially molten felsic rock outcropping in the southern part of the footwall unit. This sample is located close to the Kef Lakhal massive amphibolite unit and was sampled in contact with a highly altered actinolite thick band oriented along the main foliation.

The locality 4, close to Sidi Semhout, exposes fine-grained ultramylonites displaying small lenses of mafic and ultramafic rocks (VN16d), oriented along the foliation. A leucocratic amphibolite (VN14a) has also been sampled along the western contact with the Kef Lakhal complex.

In the thin-section description below, samples are presented according to their protolith nature: felsic (igneous), sedimentary and mafic or ultramafic.

4.1.2. Thin-section description

Felsic rocks: Diatexite VN21 presents a porphyroclastic texture (Fig. 3a) mainly composed of feldspar (orthoclase and plagioclase), quartz, biotite, and white mica porphyroclasts. Some scarce garnets have been also observed. K-feldspar is deformed as demonstrated by the occurrence of twisted twins and also contains quartz xenomorphic inclusions. Coarse biotite crystals outline the foliation and are associated to a second generation of smaller biotite at grain boundaries. Both types are partly destabilized and often associated to fibrolite. Rare late light green chlorite has also been observed. Porphyroclasts of white mica, less abundant than biotite, display mica-fish features and late biotite exsolutions.

Orthogneiss VN24d shows a protomylonitic porphyroclastic texture. The main paragenesis contains quartz, feldspar, few micas (mainly biotite and muscovite) and, rare garnets (Fig. 3b). Rare inclusions of primary mica have been observed into garnet. Orthoclase feldspar megablasts show myrmekites at its rim and quartz inclusions in its core. Polycrystalline quartz ribbons mark the foliation. Garnet is relatively small (*c*. 150–200 mm) and rare, with tails mainly formed by biotite crystallized during the latest stage of metamorphism.

Sediments: Garnet micaschists VN24b, VN25b and VN25c are made of garnet, white mica, biotite, feldspar and quartz. For VN24b, fibrolite and andalusite have also been observed as well as fluid

inclusions into garnet. Tourmaline crystals have been identified. It is noteworthy that a 10-cm thick tourmaline vein, adjacent to this sample, has been observed in the field. Rare kyanite is observed often constituting microdomains with white mica. VN25b and VN25c display garnet with biotite tails more or less chloritized (Fig. 3c). The core of garnet is rich in quartz and fluid inclusions, which are not observed in the rim. White micas are partly recrystallized into biotite associated to fibrolite. Very small zones with sillimanite and poecilitic andalusite have been also observed. Prismatic rutile is present. Another type of garnet contains an exsolved acicular rutile network in its core and does not display other mineral inclusions.

Mafic/ultramafic rocks: VN25a is an amphibolite containing xenomorphic brown amphibole, quartz, feldspar, rare rutile and relics of garnet (Fig. 3d). The texture is porphyroclastic. Grains of amphiboles are elongated and highly deformed with numerous fractures along clivage plans. Quartz grains display recrystallization features (sub-euhedral shapes associated to sharp rims).

VN26 is a garnet amphibolite lens located at the contact zone with the Kef Lakhal complex (Fig. 1b). Its metamorphic paragenesis is made of brown amphibole, feldspar, rutile, garnet and scarce quartz. It displays a porphyroclastic texture (Fig. 3e). Some garnet crystals are cataclased. Brown amphibole is often destabilized in actinote. The garnet rims contain aligned prismatic rutile, probably outlining a former foliation.

Similarly VN8 sample is a garnet amphibolite with quartz, amphibole and garnet porphyroclasts (up to 1 cm). Leucocratic layers (feldspar and quartz) are dominant in this rock. Most quartz crystallized as ribbons marking the foliation. Garnet is highly recrystallized and presents rotation figures. Some smaller polygonal garnets are also observed and possibly represent a second generation. As in most amphibolites, green and brown amphiboles have been observed. Titanite is also present mainly located around garnet and coexisting with green amphibole. This sample displays some rare occurrences of relic pyroxene.

VN14a and VN16d are leucocratic amphibolites. They contain numerous quartz, feldspar, amphibole porphyroclasts, titanite and few clinopyroxenes. The texture is porphyroclastic and a compositional bedding (with an alternation of mafic and leucocratic minerals) emphasizes the foliation. Both samples display green amphibole and titanite crystallized at the expense of garnet. VN14a contains numerous highly deformed garnets rich in oxide inclusions. Quartz crystallizes in interstitial sites.

VN32a metaperidotite (Fig. 3f) contains numerous secondary euhedral green amphiboles. Some preserved areas in the rock present relics of olivines consumed in serpentine and/or amphibole and small clinopyroxenes. Orthopyroxene is deformed and fractured. Small quartz–feldspar veinlets crosscut the sample and suggest late fluid circulation.

VN24a is a coarse-grained metaperidotite cut by talc veins and displaying centimetre-sized subhedral orthopyroxene, clinopyroxene and almost fully serpentinized olivine grains set up in a matrix of talc, brucite and actinolite.

4.2. Whole-rock chemistry

4.2.1. Major elements

Felsic rocks: The two felsic rocks analysed (diatexite VN21 and orthogneiss VN24d) are SiO_2-rich (69.2 and 75.2 wt% respectively) and display a high alumina saturation index (A/CNK = 1.31 and 1.19) characteristic of peraluminous granitoids. In the TAS diagram (Fig. 4a; Lebas et al., 1986), both samples plot in the granite field of the sub-alkaline series. In the AFM diagram they fall in the calc-alkaline domain (Fig. 4b; Irvine and Baragar, 1971).

Sediments: The micaschists (VN24b VN25b and VN25c) show high and homogeneous SiO_2 and Al_2O_3 contents (ranging from 66.7

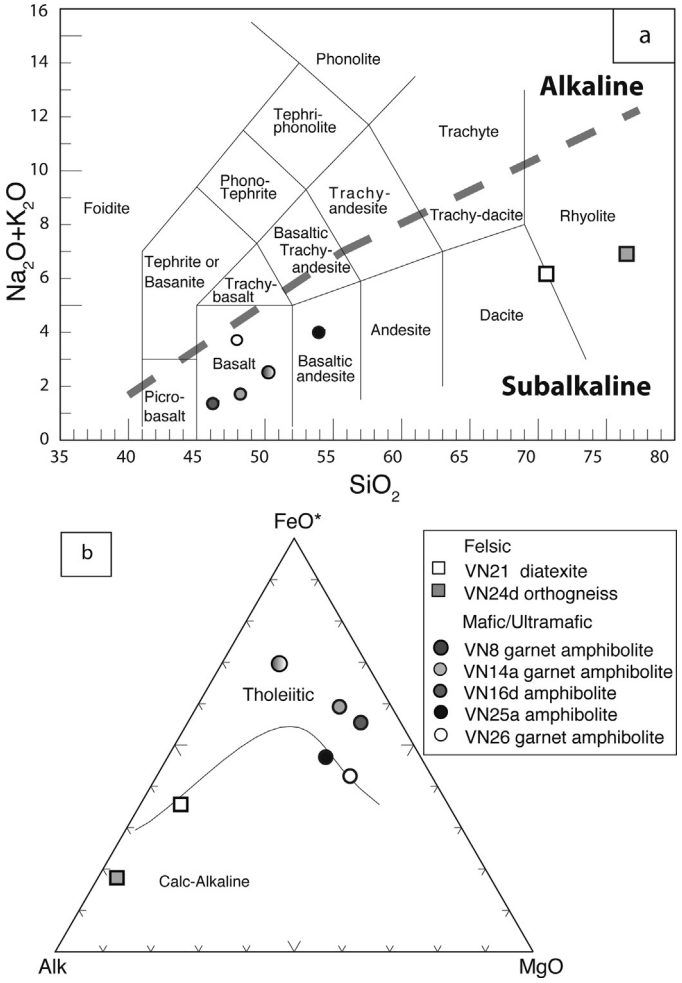

Fig. 4. Whole-rock discriminant diagrams for felsic and mafic samples: (a) $Na_2O + K_2O$ vs SiO_2 after Lebas et al. (1986); (b) AFM diagram after Irvine and Baragar (1971). FeO*: Fe total; Alk: $Na_2O + K_2O$.

to 68.6 wt% and from 14.86 to 16.97 wt% respectively, see Table 1). They are classified as shale in the diagram of Herron (1988) (not shown).

Mafic–ultramafic rocks: The amphibolite lenses (VN8, VN14a, VN16d, VN25a and VN26) and the two ultrabasic rocks (VN24a and VN32a) have low SiO_2 (from *c.* 43.0 to 52.5 wt%) and TiO_2 (from 0.40 to 1.75 wt%) contents (Table 1). The peridotite VN24a displays the lowest SiO_2 (*c.* 43%), TiO_2 (0.04 wt%) and CaO (1.76 wt%) contents. This sample exhibits a high loss on ignition of 14.4% suggesting it has been hydrolysed or carbonated, in agreement with the occurrence of abundant brucite, talc and serpentine (Table 1). In the TAS diagram (Fig. 4a; Lebas et al., 1986), the amphibolites plot in the basalt field of the sub-alkaline series. The amphibolite VN25a is located in the basaltic–andesite field. In the AFM diagram (Fig. 4b; Irvine and Baragar, 1971), the amphibolites plot either on the line separating the calc-alkaline and tholeiitic domains (VN25a and VN26) or in the tholeiitic field (VN8, VN14a and VN16d).

4.2.2. Trace elements

Felsic rocks: Both samples (orthogneiss and diatexite) display a moderately fractionated chondrite-normalized REE pattern (La/Yb_N = 5.2–7.9 and Gd/Yb_N = 1.5–1.7, Fig. 5a, Table 1) with a pronounced Eu negative anomaly (Eu* = 0.37–0.49). The primitive-mantle normalized patterns show enrichments in LILE such as Rb, Th and U, over marked depletions in HFS elements (Nb, Ta), Ba and Sr (Fig. 5b). A positive Pb spike is also observed.

Sediments: The micaschists (VN24b, VN25b and VN25c) display similar chondrite-normalized REE patterns (Fig. 5c) characterized by a moderate LREE enrichment (La/Yb_N ranging from 7.3 to 11.6), flat HREE (Gd/Yb_N ranging from 1.3 to 1.8) and a negative Eu anomaly (Eu/Eu* ranging from 0.60 to 0.63). In the primitive mantle-normalized multi-element diagram, these three samples display negative Ba, Nb, Ta and Sr anomalies, but no Zr–Hf depletion (Fig. 5d).

Mafic–ultramafic rocks: The amphibolite lenses (VN8, VN14a, VN16d, VN25a and VN26) display flat (VN25a, $La/Yb_N = 1.07$) to

Table 1
Whole-rock major and trace element concentrations of felsic, sedimentary and mafic/ultramafic samples. LOI: loss on ignition. $A/CNK = [Al_2O_3/(CaO + Na_2O + K_2O)]$. $Eu/Eu^* = [Eu/\sqrt{(Sm * Gd)}] \times 100$. La/Yb_N and Gd/Yb_N normalized to chondrite after Sun and McDonough (1989).

Majors and trace elements on whole rock						
Classification		Felsic		Sediment		
Sample		VN21	VN24d	VN24b	VN25b	VN25c
Lithology		Diatexite	Orthogneiss	Micaschist	Micaschist	Micaschist
Localization (UTM)		32S	32S	32S	32S	32S
		381,554.06 m E	385,118 m E	385,118 m E	385,118 m E	385,118 m E
		4,089,021.90 m N	4,090,032 m N	4,090,032 m N	4,090,032 m N	4,090,032 m N
Altitude (m)		349	5	5	5	5
Major element	SiO_2	69.22	75.19	66.83	66.72	68.63
(%)	Al_2O_3	15.01	12.96	16.97	15.83	14.86
	Fe_2O_3	4.37	1.76	7.21	7.98	8.47
	MnO	0.06	0.02	0.08	0.07	0.08
	MgO	0.93	0.35	1.10	1.29	1.28
	CaO	1.85	0.88	0.43	0.27	0.40
	Na_2O	2.57	3.12	0.17	0.15	0.15
	K_2O	3.62	3.79	3.56	2.53	2.84
	TiO_2	0.68	0.27	0.90	0.82	0.79
	P_2O_5	0.20	0.16	0.16	0.15	0.14
	PF	1.39	1.06	3.16	4.40	2.20
	Total	99.88	99.56	100.57	100.19	99.82
	A/CNK	1.31	1.19	–	–	–
Trace element	Ba	467.800	246.300	495.900	339.200	432.900
(ppm)	Be	1.960	1.440	1.750	1.910	1.380
	Ce	78.300	39.720	71.240	91.300	72.850
	Cs	4.740	2.130	4.460	5.770	3.440
	Cu	7.070	9.900	69.310	22.630	42.120
	Dy	6.480	5.070	5.760	5.070	5.050
	Er	3.430	2.620	3.290	2.700	2.720
	Eu	1.190	0.580	1.200	1.320	1.190
	Ga	19.670	15.320	23.870	22.280	21.530
	Gd	6.860	4.620	5.480	5.910	5.290
	Ge	1.780	1.530	1.640	1.750	1.620
	Hf	6.150	3.600	7.420	6.640	7.390
	Ho	1.230	0.970	1.170	0.950	0.970
	La	36.790	18.490	35.330	45.150	35.740
	Lu	0.490	0.370	0.530	0.430	0.430
	Nb	12.770	6.490	15.240	13.420	13.520
	Nd	36.130	19.310	31.440	39.530	31.620
	Ni	17.900	9.140	67.380	44.320	61.810
	Pb	20.970	13.230	4.830	4.750	4.380
	Pr	9.410	4.990	8.390	10.550	8.500
	Rb	151.700	158.600	171.000	130.400	134.500
	Sm	7.910	4.900	6.300	7.530	6.260
	Sn	4.820	4.670	7.450	6.870	6.560
	Sr	152.900	99.910	26.100	16.250	29.080
	Ta	1.420	0.750	1.410	1.230	1.200
	Tb	1.080	0.830	0.910	0.870	0.830
	Th	14.420	10.360	11.590	14.130	11.980
	Tm	0.520	0.400	0.510	0.420	0.430
	U	2.970	2.970	3.170	3.310	2.700
	V	47.360	16.530	109.800	106.700	95.940
	W	2.630	2.510	2.340	2.310	1.930
	Y	37.460	28.980	33.830	29.170	28.950
	Yb	3.330	2.530	3.460	2.790	2.880
	Zn	60.240	17.360	66.690	49.010	51.780
	Zr	238.400	120.400	283.000	256.800	294.100
	Li	–	7.390	–	–	–
	La/Yb_N	7.925	5.246	7.331	11.604	8.892
	Gd/Yb_N	1.705	1.513	1.312	1.753	1.519
	Eu/Eu*	0.494	0.374	0.624	0.605	0.633
	REE	193.150	105.392	175.005	214.537	174.758
	Ce/Pb	3.734	3.002	14.749	19.221	16.632
	Th/Yb	4.330	4.095	3.350	5.065	4.160
	Zr/Th	16.53	11.62	24.42	18.17	24.55

Table 1 (*Continued*)

Majors and trace elements on whole rock								
Classification		Mafic–ultramafic						
Sample		VN8	VN14a	VN16d	VN24a	VN25a	VN26	VN32a
Lithology		Garnet amphibolite	Amphibolite	Amphibolite	Peridotite	Amphibolite	Garnet amphibolite	Peridotite
Localization (UTM)		32S	32S	32S	32S	32S	32S	32S
		381,535 m E	381,562.00	381,158 m E	385,118 m E	385,118 m E	382,891.91 m E	382872 m E
		4,089,033 m N	4,090,585.00	4,090,689 m N	4,090,032 m N	4,090,032 m N	4,090,572.23 m N	4,090,072 m N
Altitude (m)		361	141	124	5	190		229
Major element (%)	SiO_2	49.24	46.79	45.08	42.97	52.47	48.04	47.90
	Al_2O_3	19.43	15.02	16.90	2.45	15.36	17.67	11.30
	Fe_2O_3	10.45	10.26	9.50	8.33	10.40	10.80	8.79
	MnO	0.25	0.15	0.15	0.09	0.17	0.21	0.13
	MgO	1.64	4.67	5.64	28.75	6.64	9.34	14.26
	CaO	14.26	17.77	18.86	1.76	7.37	6.94	11.66
	Na_2O	1.89	1.12	0.42	0.06	3.31	3.48	1.66
	K_2O	0.59	0.57	0.90	< L.D.	0.66	0.48	1.15
	TiO_2	1.09	1.36	0.93	0.04	1.75	1.28	0.40
	P_2O_5	0.21	0.41	0.21	< L.D.	0.21	0.29	< L.D.
	PF	1.15	1.61	1.03	14.41	1.71	1.69	2.08
	Total	100.18	99.73	99.62	98.86	100.05	100.24	99.34
Trace element (ppm)	Ba	26.260	40.760	134.290	11.640	62.230	80.700	121.290
	Be	15.870	1.680	–	–	5.900	–	–
	Ce	94.150	106.200	92.780	6.580	16.990	45.610	7.550
	Cs	1.490	12.680	13.150	0.440	0.633	0.600	5.510
	Cu	89.390	80.960	–	–	46.570	–	–
	Dy	9.770	8.980	6.210	2.550	6.860	7.740	2.400
	Er	4.560	5.260	3.110	1.400	4.000	4.260	1.420
	Eu	1.800	2.310	1.890	0.540	1.740	1.360	0.320
	Ga	21.260	29.250	–	–	20.720	–	–
	Gd	10.590	8.570	6.900	2.600	6.010	7.580	1.830
	Ge	4.690	1.810	–	–	1.880	–	–
	Hf	2.820	7.460	0.660	0.080	3.860	0.640	0.710
	Ho	1.740	1.850	1.160	0.510	1.420	1.560	0.490
	La	45.680	54.580	47.570	1.820	6.020	18.880	3.330
	Lu	0.660	0.730	0.450	0.210	0.620	0.590	0.210
	Nb	27.230	19.720	18.470	0.590	3.160	4.630	5.060
	Nd	43.860	48.510	43.070	6.860	14.560	26.440	4.640
	Ni	54.510	89.340	81.550	2445.670	117.800	92.830	840.950
	Pb	5.790	10.450	6.150	0.520	7.530	8.360	6.300
	Pr	11.290	12.710	10.830	1.180	2.780	5.640	1.000
	Rb	32.320	23.170	38.150	0.360	13.100	13.550	30.310
	Sm	11.130	9.720	7.440	2.000	5.020	6.170	1.320
	Sn	37.210	4.230	–	–	3.380	–	–
	Sr	365.300	454.900	325.130	22.682	154.300	209.370	143.330
	Ta	5.220	1.860	1.730	0.050	0.480	0.340	0.690
	Tb	1.760	1.410	1.050	0.400	1.060	1.190	0.350
	Th	24.000	14.580	13.420	0.090	1.160	4.140	1.280
	Tm	0.680	0.790	0.450	0.200	0.610	0.590	0.220
	U	20.560	5.290	2.830	0.100	2.550	0.380	0.660
	V	121.900	282.100	192.300	56.270	261.500	207.390	76.580
	W	2.230	0.320	1.580	0.210	4.110	0.350	0.260
	Y	53.510	57.390	37.290	16.050	41.030	47.110	15.660
	Yb	4.480	4.840	2.750	1.280	4.030	3.640	1.350
	Zn	65.770	155.000	108.430	76.940	100.300	94.470	180.550
	Zr	100.100	286.400	14.370	2.040	146.000	16.760	11.120
	Li	–	15.340	14.440	4.640	8.300	20.340	10.460
	La/Yb_N	7.312	8.084	12.417	1.024	1.071	3.717	1.769
	Gd/Yb_N	1.955	1.463	2.078	1.685	1.234	1.720	1.123
	Eu/Eu^*	0.507	0.774	0.806	0.730	0.970	0.610	0.631
	REE	242.139	266.449	225.660	28.149	71.742	131.258	26.425
	Ce/Pb	16.261	10.163	15.086	12.654	2.256	5.456	1.198
	Th/Yb	5.357	3.012	4.880	0.070	0.288	1.137	0.948
	K_2O/TiO_2	0.54	0.42	0.97	–	0.38	0.38	2.88

LREE enriched (VN8, VN14a and VN16d, La/Yb_N = 7.3–12.4 respectively) patterns (Fig. 5e). Sample VN26 exhibits an intermediate LREE enriched pattern (La/Yb_N = 3.7). All amphibolites are characterized by a patent negative Eu anomaly (Eu/Eu* = 0.5–0.8), except VN25a (Eu/Eu* = 0.97). The ultrabasic rocks display flat REE patterns, either slightly LREE depleted (VN24a) or slightly LREE enriched (VN32a) (Fig. 5g). Both have a significant negative Eu anomaly (Eu/Eu* = 0.63–0.73). Incompatible element patterns (Fig. 5g) are characterized by a general LILE enrichment with pronounced depletion in Ba (except sample VN24a), Nb, Zr and Hf. All samples yield a slight to pronounced positive Pb spike (Fig. 5f–h).

4.3. *Mineral chemistry: major and trace elements*

Tables for major elements in minerals are available as Supplementary Materials 1a (garnet), 1b (amphibole), 1c (feldspar), 1d (white mica), 1e (Fe–Mg mica) and 1f (pyroxene). The micas results are available only as Supplementary Material 2. Tables

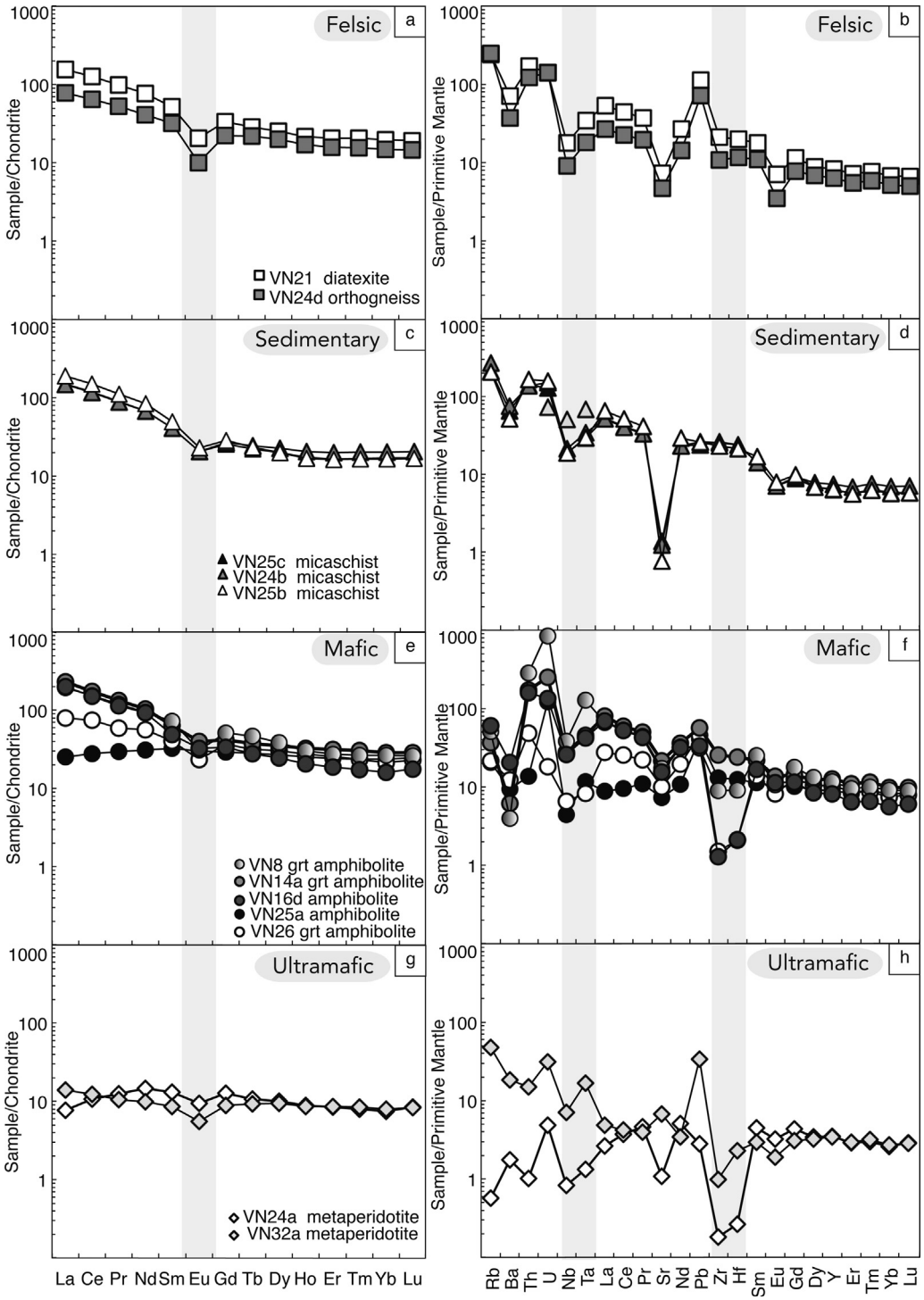

Fig. 5. Chondrite-normalized REE and Primitive Mantle-normalized trace element patterns for felsic (a, b), sedimentary (c, d), mafic (e, f) and ultramafic (g, h) samples. Normalizing values after Sun and McDonough (1989).

for trace elements in minerals are available as Supplementary Materials 3a–d.

4.3.1. Garnet

Felsic rocks: Garnet from VN21 has a high spessartine composition, ranging from 8.5% to 11.5% from core to rim. Garnet from the orthogneiss VN24d is almandine-type (Fig. 6a). It shows low compositional variations in iron content, (i.e. <5%) with, nevertheless a rim characterized by a higher spessartine content and a lower grossular composition (i.e. 16%Sps–3%Grs) than the core (i.e. 7–8%Sps–6–9%Grs) suggesting the preservation of prograde conditions into the garnet core. The trace element patterns of garnet from both rocks display pronounced Eu and Ba negative anomalies that could be related to coeval feldspar crystallization (Fig. 7a and b).

Sediments: Garnet from VN24b and VN25b is mainly of almandine-type (72–86%Alm–13–22%Prp) with a compositional zonation characterized by an increase in iron content from the core

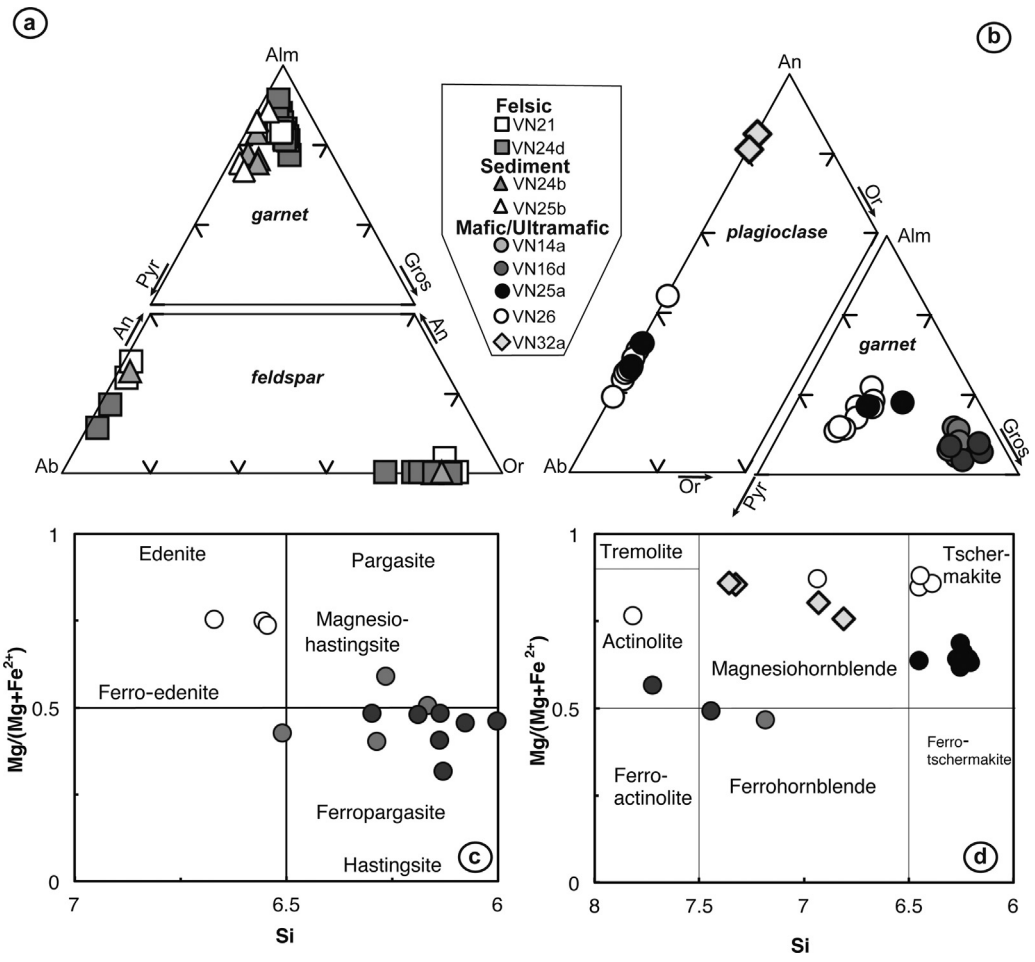

Fig. 6. (a, b) Ternary plots showing the composition of the garnet and feldspar from felsic rocks and sediments (a) and mafic and ultramafic rocks (b). Alm: almandine, Pyr: pyrope, Gros: grossulaire, An: anorthite, Ab: albite, Or: orthose. (c, d) $Mg/(Mg+Fe^{2+})$ vs Si discriminant diagrams for amphibole. (c) $Ca_B \geq 1.50$; $(Na+K)_A \geq 0.50$ and $Ti < 0.50$; (d) $Ca_B \geq 1.50$; $(Na+K)_A < 0.50$ and $Ca_A < 0.50$. Classification diagrams for amphibole after Leake et al. (1997).

towards the rim (i.e. from 76% to 82%Alm for VN24b and from 73% to 86%Alm for VN25b) along with a decrease of spessartine component (Fig. 6a). Such zoning indicates that the garnet rims were formed under a higher temperature than the core and thus suggests a reheating process. Garnet from both rocks yields close to similar trace element patterns with a strong HREE/LREE enrichment and nearly flat to decreasing HREE patterns (Fig. 7c). Some crystals show a chemical zonation with an increase of total REE content from core to rim (Fig. 7c).

Mafic–ultramafic rocks: VN26 garnet shows a core-rim gradual zonation with a strong increase in iron (from 50.8% to 58.8%Alm), concomitant with a decrease in Mg (from 21.4% to 34.3%Prp) and Mn (from 4.8% to 1.1%Sps) from core to rim (Fig. 6b). The REE patterns for VN26 garnet show a strong HREE/LREE enrichment (Fig. 7e and f), combined with a HREE depletion between the inner and the outer parts of the crystals (Fig. 7e). Garnet from VN25a does not display significant variations in almandine (i.e. 55.6%Alm in average) or spessartine contents. Variations are observed in grossular and pyrope content, with values ranging from ~15% to ~25% for both.

Garnet from VN14a and VN16d broadly displays similar major element features (Fig. 6b) with a high almandine (from 43.2% to 50.4%Alm) and grossular content (from 38.1% to 47.7%Grs) and no significant core-rim variations (Fig. 6b). The REE patterns of garnet from VN16d have a similar shape to those from VN26 and VN25a, with a slight negative Eu anomaly (Fig. 7e and f). Garnet from VN14a presents a REE pattern steadily decreasing from HREE to LREE.

4.3.2. Amphibole

Amphiboles present two compositional trends. Amphiboles from samples VN32a, VN14a and VN16d range from actinolite to magnesio-hornblende and pargasite whereas those from samples VN25a and VN26 range from magnesio-hornblende to tschermakite (Fig. 6c and d).

VN26 amphibole shows a scattered composition between magnesio-hornblende and tschermakite (Fig. 6c and d), whereas amphibole from VN25a is more homogeneous and plots in the tschermakite field. Magnesio-hornblende presents low K and Si contents associated to high Al^{IV} and intermediate Na content. Amphibole from all mafic samples, except two analyses on VN32a and one on VN14a, is enriched in total Al ($Al^{IV} > 1.0$) suggesting a temperature range equivalent to that of the staurolite–kyanite zone in the metapelites (i.e. $T > 600$ °C, Caby et al., 2001). This conclusion is in agreement with the fact that the studied amphibolites are enclosed in garnet-rich micaschists and have undergone similar metamorphic conditions. The Al^{IV}/Al^{VI} ratios yield values from 1.45 to 2.8 suggesting that all the analysed crystals are metamorphic and record an evolution from high-grade amphibolite-facies to lower-grade metamorphism (Fleet and Barnett, 1978).

Overall the REE distribution for amphibole presents various trends with no clear strong relationship with major element composition (Fig. 7k and l). The first type is characterized by a concomitant impoverishment in LREE/MREE and HREE/MREE that confers a convex shape to the pattern. This convex pattern is found

in tschermakite from VN26 garnet amphibolite and in magnesiohornblende from sample VN32a. The second type is characterized by a flat MREE–HREE distribution and a LREE depletion (e.g. sample VN25a) and often corresponds to tschermakite amphibole composition. In sample VN16d, such pattern is, for some analyses, combined with a strong Eu negative anomaly (Fig. 7k) and often associated to actinolite, which is in agreement with a late metamorphic imprint in the field of plagioclase. Another type of pattern corresponds to ferropargasite and magnesiohornblende (VN14a, VN16d, VN32a) and is characterized by depletion from HREE to LREE. All amphibole analyses show Zr–Hf and Th negative anomalies. Only tschermakite displays strong combined Nb–Ta negative anomalies. This pattern is close to similar to that of coexisting pyroxene (see below) suggesting these amphiboles could derive from destabilization of pyroxene.

4.3.3. Feldspar

Felsic rocks and sediments: Feldspar from felsic rocks display a solid solution between albite and orthoclase, with highly variable orthoclase content (Fig. 6a). Only feldspar from VN24b has been studied and shows variable compositions from orthoclase (94%) to albite (96%) (Fig. 6a).

REE chondrite-normalized patterns of feldspar from both rock-types are slightly LREE enriched (Fig. 7g and h) and show no Eu positive anomaly, typically observed in K-feldspar and plagioclase. The later can be ascribed to extensive fractionation of feldspar or to oxidizing conditions (Weill and Drake, 1973). Considering the lack of coeval Ba and Sr anomalies, the second alternative is a more likely explanation. The PM-normalized incompatible element patterns are characterized by negative troughs in Nb and Ta, and positive Pb spikes (Fig. 7g and h).

Mafic–ultramafic rocks: Feldspar from mafic and ultramafic samples displays variable compositions from albite to anorthite, with feldspar from VN32a displaying the highest anorthite content (>63An%, Fig. 6b).

Feldspar from VN26 overall displays a more sodic composition (67–82Ab%) but two analyses corresponding to anti-perthitic exsolutions show a low albite content (<38Ab%) combined to a high K content (~49F_K%).

The REE patterns of feldspars are characterized by strong LREE enrichment and a patent positive Eu anomaly (Fig. 7i). The PM-normalized trace element spectra show strong Th, Nb, Ta and Zr–Hf negative anomalies combined with positive Sr and Pb spikes (Fig. 7j). These trace elements patterns are strikingly different from those observed for feldspar from felsic rocks and sediments.

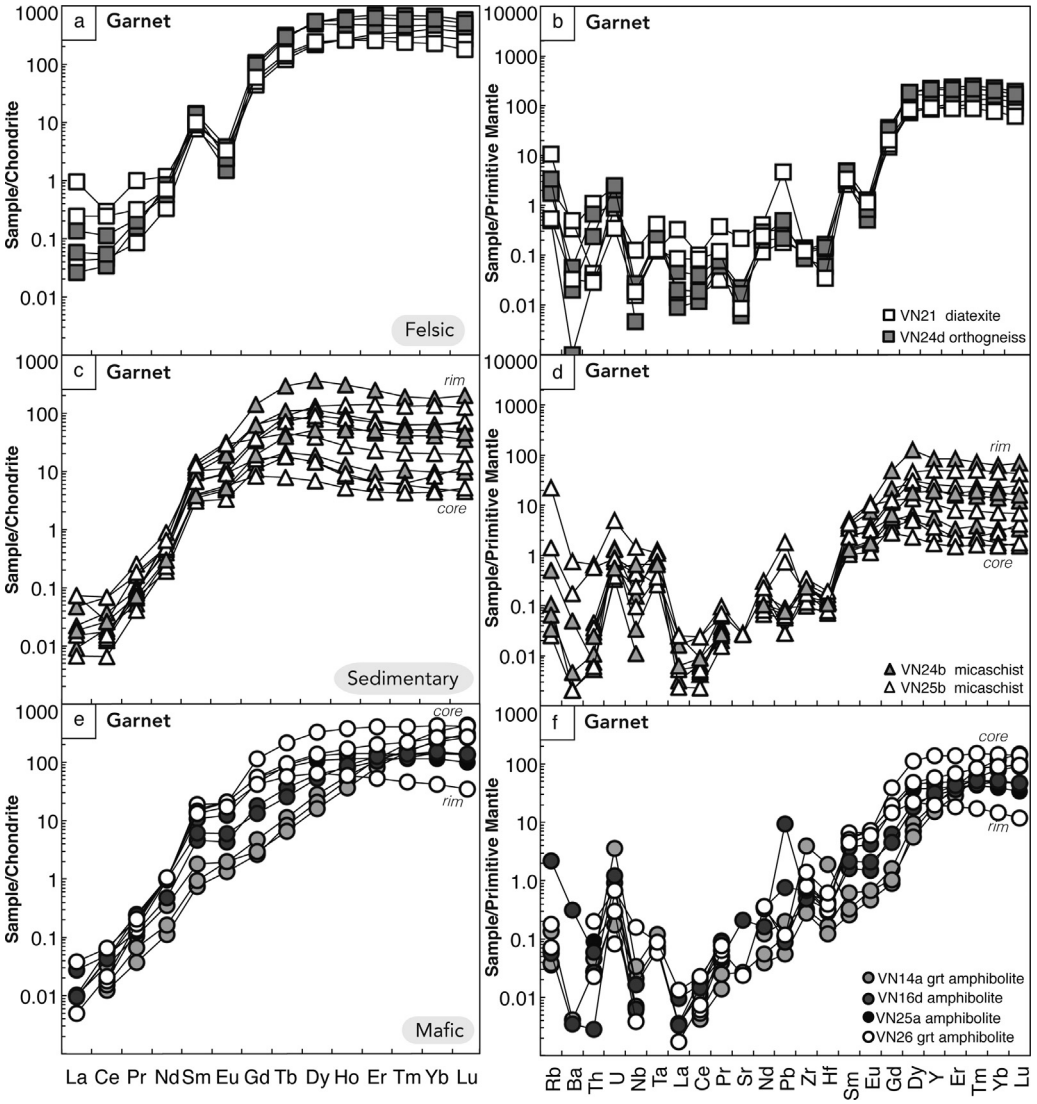

Fig. 7. Chondrite-normalized REE and Primitive Mantle-normalized trace element patterns for minerals from felsic, sedimentary, mafic and ultramafic samples. Normalizing values after Sun and McDonough (1989).

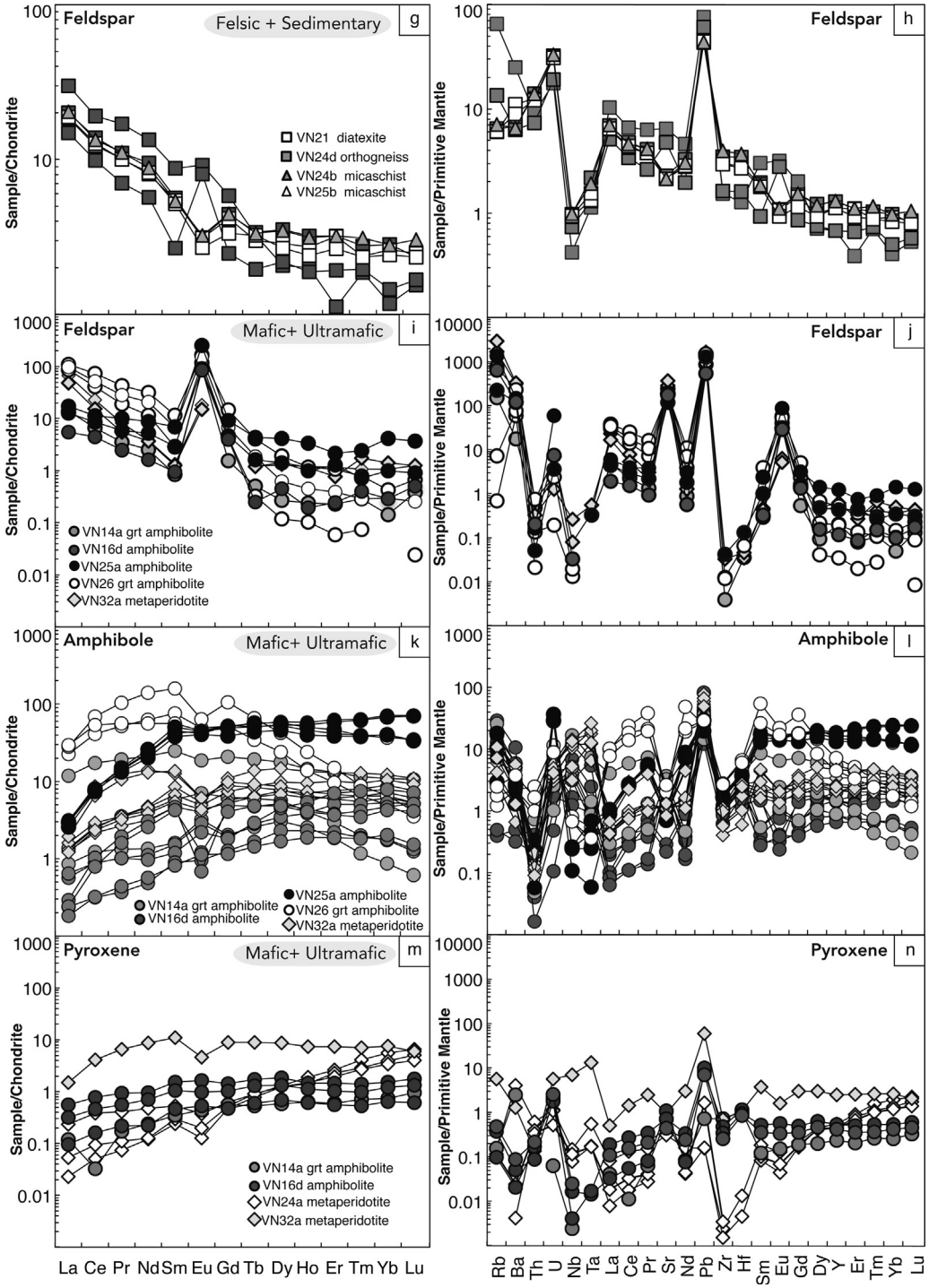

Fig. 7. (*Continued*).

4.3.4. Pyroxene

Pyroxene in mafic and ultramafic lithologies is rarely preserved, and has been analysed only in four samples. In sample VN24a its composition corresponds to an orthopyroxene, whereas other samples display clinopyroxene composition. In the ultramafic rock VN32a, the pyroxene is a pigeonite. The amphibolites VN16d and VN14a contain pyroxene with an augite composition. CPX for most samples show LREE depleted patterns (Fig. 7m). A marked negative Eu anomaly is only observed for sample VN32a. OPX from VN24a shows a steadily decreasing pattern from HREE to LREE with marked negative Eu and Zr–Hf anomalies (Fig. 7m and n). Clinopyroxene from VN14a displays a Ce negative anomaly.

4.3.5. Temperature estimates

Temperature estimates have been obtained for the amphibolites VN14a, VN25a, and VN26, and for the orthogneiss VN24d and the micaschist VN25b using either major element in situ analyses of minerals or Zr-in-rutile thermometry after Ferry and Watson (2007) (Supplementary Material 3e).

According to the garnet-biotite thermometer (calibration after Ferry and Spear, 1978; Hodges and Spear, 1982), peak temperatures, estimated with an error of ±50 , 686–727 and 584–621 °C (at 7–10 kbar) were calculated for the diatexite VN21 and for the orthogneiss VN24d respectively. Rutile from the micaschist VN25b provides a Zr-in-rutile temperature of 607 ± 17 °C in

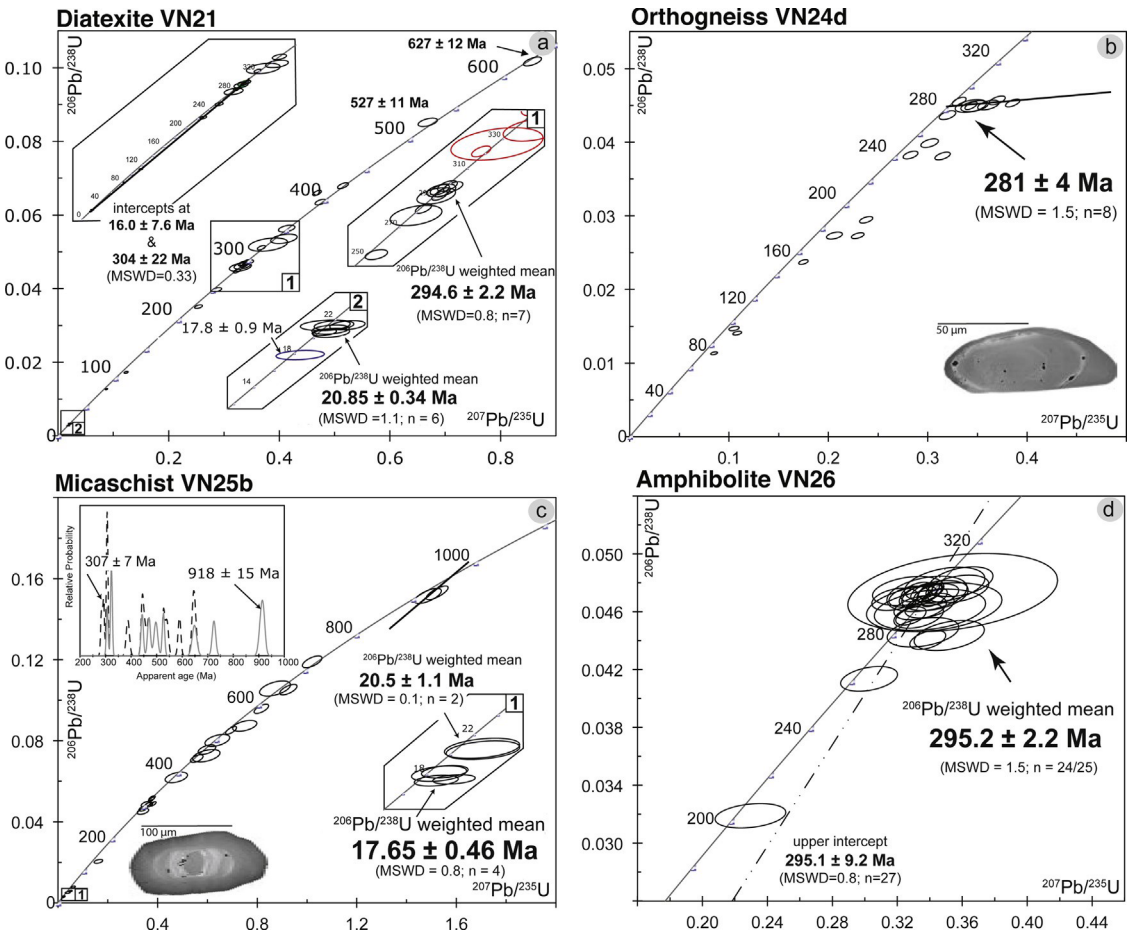

Fig. 8. Concordia plot for LA-ICP-MS U-Pb analyses of zircon with scanning electron microscope (BSE) imaging of selected grains. Ellipses are 1 error.

good agreement with the temperature provided by the garnet-biotite thermometer. Plagioclase–amphibole pairs (calibration after Holland and Blundy, 1994) in amphibolites VN14a, VN25a and VN26 yield temperatures of 721–766, 670–704 and 657–703 °C (±50 °C) respectively. Rutile from the amphibolite VN26 yields a temperature of 613 ±48 °C, slightly but significantly lower than the temperature provided by the plagioclase–amphibole pair in the same rock.

5. Geochronology

5.1. U–Pb geochronology

5.1.1. Diatexite VN21

Zircons from this sample display a prismatic euhedral to subhedral shape in agreement with a primary magmatic origin for the protolith of the diatexite. Observed in back-scattered electron mode, most grains yield a featureless internal structure sometimes with remains of a faint oscillatory zoning. In some grains, a massive, unzoned rim can be observed. The blurred internal structure of these grains and the occurrence of a rim both suggest that the grains have been subjected to a metamorphic event. Wherever possible, U–Pb analyses were conducted on both the central part of the grain and on the rim. Reported in the Concordia diagram, the analyses of the central part of the grains display a large scattering with ages broadly ranging from 100 to 650 Ma. Some of the oldest ages are clearly associated with a core structure, which indicates that they reflect the age of source rocks or of deep-seated components assimilated during emplacement of the protolith of the diatexite. These grains include concordant ages at 321 ±6, 327 ±18, 397 ±8, 424 ±8, 527 ±11 and 627 ±12 Ma (2) (Fig. 8a). The most important batch includes seven analyses, which define a consistent concordant population with a $^{206}Pb/^{238}U$ weighted mean age of 294.6 ±2.2 Ma (MSWD = 0.8). The latter is related to the age of the protolith that suffered metamorphism and partial melting. This set apart, the youngest ages are from featureless overgrowths with high U contents (1034 ppm in average for the 7 overgrowths analysed) and low Th/U ratios (lower than 0.07 and generally lower than 0.02) (Table 2). These analyses plot concordantly at around 20 Ma. Six out of seven of these analyses provide a $^{206}Pb/^{238}U$ weighted mean age of 20.85 ±0.34 Ma (MSWD = 1.1), which we relate to the high temperature metamorphic event responsible for partial melting of the protolith and the growth of the zircon rim. One analysis is slightly but significantly younger at 17.8 ±0.9 Ma (2).

5.1.2. Orthogneiss VN24d

Zircons from this sample display a prismatic euhedral to subhedral shape. Reported in the Concordia diagram, analyses yield various degrees of discordance (Fig. 8b) with $^{206}Pb/^{238}U$ ages broadly ranging from *c*. 80 to 300 Ma (Table 2). In addition, many analyses yield variable $^{207}Pb/^{206}Pb$ ratios suggesting they contain a significant proportion of common or inherited lead shifting the points on the right of the Concordia. The combination of these two phenomena (discordance and common lead/inheritance) hampers any age calculation using all analyses. A batch of analyses however, provides consistent $^{206}Pb/^{238}U$ ages at around 280 Ma and defines a reverse discordia with a lower intercept age of 281 ± 4 Ma (*n* = 8;

Table 2
Laser ablation ICP-MS U–Th–Pb isotopic data for zircons from lithologies of the Edough Massif (NE Algeria). c = core; r = rim.

															Apparent ages (Ma)			
			Pb* (ppm)	Th (ppm)	U (ppm)	Th/U	208Pb/ 206Pb	207Pb/ 206Pb	±	207Pb/ 235U	±	206Pb/ 238U	±	Rho	206Pb/ 238U	±	207Pb/ 206Pb	±
Classification	Felsic	#1-1, c	69.4	43.6	1650	0.03	0.01	0.0520	0.0010	0.3358	0.0060	0.0469	0.0005	0.56	295.4	2.9	283	45
Lithology	Diatexite	#1-2	34.4	42.2	734	0.06	0.02	0.0522	0.0010	0.3676	0.0060	0.0511	0.0005	0.58	321.4	3.0	293	41
Sample	VN21	#1-3, r	13.0	15.5	845	0.02	0.02	0.0518	0.0014	0.1232	0.0031	0.0173	0.0002	0.45	110.3	1.3	276	62
		#2-1, r	1.4	5.4	548	0.01	–	0.0485	0.0053	0.0185	0.0020	0.0028	0.0001	0.24	17.8	0.4	123	238
		#2-2, c	21.9	19.7	447	0.04	0.01	0.0515	0.0008	0.4681	0.0065	0.0660	0.0006	0.64	411.8	3.6	262	36
		#3-1, r	4.6	10.8	1189	0.01	0.01	0.0482	0.0036	0.0215	0.0015	0.0032	0.0001	0.31	20.8	0.4	108	165
		#4-1, r	4.8	17.7	1337	0.01	0.00	0.0474	0.0034	0.0216	0.0015	0.0033	0.0001	0.31	21.3	0.4	70	160
		#5-1, r	31.5	122.7	743	0.17	0.07	0.0523	0.0009	0.3233	0.0051	0.0448	0.0004	0.61	282.5	2.6	299	40
		#5-2, c	47.3	147.9	1108	0.13	0.05	0.0524	0.0011	0.3417	0.0062	0.0473	0.0005	0.56	297.8	3.0	302	45
		#6-1	33.3	173.0	305	0.57	0.19	0.0613	0.0011	0.8624	0.0134	0.1021	0.0010	0.63	626.5	5.8	648	37
		#7-1	12.5	23.1	267	0.09	0.03	0.0522	0.0015	0.3369	0.0092	0.0468	0.0006	0.45	294.9	3.6	293	66
		#8-1	6.3	16.9	125	0.14	0.06	0.0530	0.0043	0.3797	0.0289	0.0520	0.0015	0.37	326.5	9.0	328	173
		#9-1	9.2	12.6	272	0.05	0.02	0.0524	0.0014	0.2871	0.0071	0.0397	0.0005	0.46	251.0	2.8	303	59
		#10-1	20.1	14.8	456	0.03	0.01	0.0531	0.0010	0.3461	0.0061	0.0472	0.0005	0.56	297.3	2.9	335	43
		#11-1, r	4.2	15.4	1223	0.01	0.00	0.0492	0.0035	0.0215	0.0015	0.0032	0.0001	0.32	20.4	0.4	159	160
		#12-1	29.4	44.6	691	0.06	0.02	0.0526	0.0009	0.3356	0.0049	0.0462	0.0004	0.62	291.3	2.6	312	37
		#13-1	11.8	42.8	272	0.16	0.06	0.0522	0.0020	0.3330	0.0121	0.0462	0.0007	0.44	291.2	4.5	295	87
		#14-1	34.4	28.9	808	0.04	0.01	0.0526	0.0008	0.3381	0.0046	0.0466	0.0004	0.66	293.5	2.6	311	35
		#15-1, r	24.5	62.1	848	0.07	0.03	0.0507	0.0033	0.0231	0.0014	0.0033	0.0001	0.34	21.3	0.4	225	144
		#16-1, r	4.5	28.6	1625	0.02	0.00	0.0475	0.0024	0.0209	0.0010	0.0032	0.0001	0.33	20.5	0.3	73	114
		#17-1	14.4	117.3	141	0.83	0.29	0.0568	0.0013	0.6683	0.0142	0.0852	0.0009	0.51	527.0	5.6	484	51
		#18-1	34.8	242.6	1170	0.21	0.39	0.0524	0.0013	0.2540	0.0058	0.0351	0.0004	0.50	222.4	2.5	303	55
		#19-1	19.6	17.6	1794	0.01	0.01	0.0500	0.0011	0.0875	0.0017	0.0127	0.0001	0.52	81.2	0.8	196	50
		#20-1	6.5	12.8	122	0.10	0.05	0.0552	0.0028	0.4083	0.0196	0.0535	0.0010	0.41	336.1	6.4	422	110
		#21-1, c	19.9	106.3	302	0.35	0.12	0.0541	0.0010	0.4745	0.0081	0.0635	0.0006	0.57	397.0	3.8	375	42
		#21-2, r	61.5	697.9	780	0.89	0.28	0.0549	0.0010	0.5151	0.0080	0.0680	0.0007	0.61	423.8	3.9	407	38
		#22-1	1.4	3.4	469	0.01	0.00	0.0462	0.0049	0.0211	0.0022	0.0033	0.0001	0.24	21.3	0.5	10	236
		#23-1	2.4	12.4	71	0.17	0.10	0.0522	0.0029	0.3176	0.0163	0.0440	0.0009	0.41	277.8	5.7	295	120
		#24-1	4.1	5.4	97	0.06	0.03	0.0535	0.0017	0.4133	0.0122	0.0559	0.0008	0.45	350.9	4.6	349	71
Classification	Felsic	#1-1	12.0	58.7	508	0.12	0.06	0.0535	0.0013	0.1749	0.0039	0.0237	0.0003	0.49	151.1	1.6	348	54
Lithology	Orthogneiss	#2-1	46.1	37.6	607	0.06	0.04	0.0531	0.0013	0.3200	0.0068	0.0437	0.0005	0.53	275.5	3.0	334	53
Sample	VN24d	#3-1	45.3	134.5	1132	0.12	0.07	0.0617	0.0011	0.3856	0.0059	0.0453	0.0004	0.63	285.7	2.7	663	37
		#4-1	6.9	38.3	328	0.12	0.08	0.0547	0.0019	0.2061	0.0065	0.0273	0.0004	0.45	173.7	2.5	400	75
		#5-1	10.2	44.9	595	0.08	0.08	0.0544	0.0019	0.0850	0.0028	0.0113	0.0002	0.43	72.7	1.0	387	77
		#6-1	9.0	51.5	223	0.23	0.08	0.0554	0.0022	0.3435	0.0129	0.0449	0.0007	0.42	283.2	4.4	430	87
		#7-1	24.2	266.7	696	0.38	0.13	0.0549	0.0014	0.3019	0.0072	0.0399	0.0005	0.50	252.0	3.0	408	57
		#8-1	26.0	114.7	720	0.16	0.06	0.0536	0.0013	0.2827	0.0061	0.0383	0.0004	0.52	242.0	2.7	354	53
		#9-1	7.5	46.6	369	0.13	0.08	0.0518	0.0022	0.1050	0.0042	0.0147	0.0002	0.41	94.0	1.5	278	95
		#10-1	13.5	77.7	368	0.21	0.09	0.0581	0.0015	0.3611	0.0088	0.0450	0.0005	0.49	284.0	3.4	533	57
		#11-1	34.9	401.8	798	0.50	0.14	0.0528	0.0010	0.3317	0.0057	0.0455	0.0005	0.59	287.1	2.8	319	43
		#12-1	40.7	506.9	929	0.55	0.15	0.0554	0.0009	0.3437	0.0051	0.0450	0.0004	0.65	283.5	2.6	428	36
		#13-1	9.4	67.4	227	0.30	0.11	0.0560	0.0019	0.3471	0.0112	0.0449	0.0006	0.43	283.0	3.8	453	75
		#14-1	22.0	182.1	653	0.28	0.12	0.0599	0.0013	0.3150	0.0063	0.0381	0.0004	0.56	241.2	2.7	598	47
		#15-1	17.4	28.6	88	0.32	0.11	0.0558	0.0020	0.1082	0.0036	0.0141	0.0002	0.45	90.0	1.4	443	79
		#16-1	15.9	25.4	79	0.32	0.11	0.0586	0.0012	0.3698	0.0067	0.0457	0.0005	0.59	287.9	3.0	554	43
		#17-1	25.4	46.6	717	0.06	0.10	0.0585	0.0015	0.2380	0.0054	0.0295	0.0004	0.53	187.2	2.2	549	54
		#18-1	14.1	121.7	550	0.22	0.12	0.0609	0.0015	0.2296	0.0052	0.0273	0.0003	0.52	173.6	2.0	635	52
Classification	Sediment	#1-1, c	107.3	378.2	1007	0.38	0.06	0.0532	0.0008	0.3747	0.0049	0.0511	0.0005	0.68	321.3	2.8	335	33
Lithology	Micaschist	#2-1	11.1	102.5	86	1.19	0.45	0.0623	0.0018	0.7503	0.0199	0.0874	0.0011	0.47	539.8	6.5	683.4	60
Sample	VN25b	#3-1	58.9	10.6	344	0.03	0.01	0.0563	0.0034	0.0614	0.0035	0.0079	0.0002	0.41	50.7	1.2	463.0	129
		#4-1, r	44.9	174.2	698	0.25	0.11	0.0512	0.0062	0.0226	0.0026	0.0032	0.0001	0.35	20.6	0.8	247.6	258
		#5-1, r	15.1	53.8	263	0.20	0.13	0.0498	0.0044	0.0194	0.0016	0.0028	0.0001	0.34	18.2	0.5	185.7	192

Table 2 (*Continued*)

														Apparent ages (Ma)			
			Pb* (ppm)	Th (ppm)	U (ppm)	Th/U	208Pb/ 206Pb	207Pb/ 206Pb	±	207Pb/ 235U	±	206Pb/ 238U	±	Rho	206Pb/ 238U	±	207Pb/ 206Pb	±
		#6-1	18.9	205.3	351	0.58	0.19	0.0533	0.0012	0.3411	0.0067	0.0465	0.0005	0.54	292.7	3.0	339.5	48
		#1-2, r	49.8	135.8	1030	0.13	0.04	0.0530	0.0008	0.3776	0.0052	0.0517	0.0005	0.66	324.8	2.9	327.9	35
		#7-1, r	16.3	28.4	1055	0.03	0.02	0.0541	0.0041	0.0202	0.0015	0.0027	0.0001	0.30	17.4	0.4	376.9	163
		#8-1	46.7	117.0	270	0.43	0.15	0.0722	0.0010	1.5229	0.0181	0.1530	0.0014	0.76	917.6	7.7	991.3	28
		#7-2, r	52.0	75.7	960	0.08	0.03	0.0567	0.0008	0.3824	0.0048	0.0489	0.0004	0.71	307.6	2.7	481.1	32
		#7-3, c	48.4	131.0	555	0.24	0.08	0.0592	0.0009	0.6953	0.0090	0.0851	0.0008	0.70	526.7	4.6	575.6	32
		#8-1	23.4	187.5	337	0.56	0.25	0.0579	0.0020	0.6400	0.0204	0.0802	0.0012	0.47	497.0	7.2	526.4	74
		#9-1, r	5.3	40.3	340	0.12	0.14	0.0504	0.0043	0.0187	0.0015	0.0027	0.0001	0.32	17.3	0.5	214.4	186
		#10-1	5.8	32.9	93	0.35	0.16	0.0557	0.0023	0.4752	0.0184	0.0619	0.0011	0.44	387.2	6.4	439.2	90
		#11-1	20.8	171.6	211	0.81	0.28	0.0574	0.0027	0.1623	0.0071	0.0205	0.0004	0.43	130.8	2.5	507.7	101
		#12-1, c	22.3	157.8	454	0.35	0.12	0.0546	0.0011	0.3650	0.0064	0.0485	0.0005	0.57	305.0	3.0	397.5	43
		#12-1, r	21.1	108.6	464	0.23	0.08	0.0548	0.0017	0.3412	0.0095	0.0452	0.0006	0.48	284.7	3.7	404.9	66
		#13-1	60.1	266.6	618	0.43	0.15	0.0619	0.0010	0.8169	0.0120	0.0957	0.0009	0.66	589.4	5.5	670.7	35
		#14-1	32.4	121.4	188	0.65	0.21	0.0712	0.0012	1.4859	0.0221	0.1514	0.0015	0.68	909.0	8.5	962.9	34
		#15-1	73.9	1383.9	255	5.44	1.92	0.0623	0.0011	1.0209	0.0161	0.1189	0.0012	0.64	724.5	6.9	683.4	37
		#16-1, r	46.5	332.5	1191	0.28	0.09	0.0492	0.0052	0.0189	0.0019	0.0028	0.0001	0.36	18.0	0.6	155.5	231
		#17-1	30.5	67.2	494	0.14	0.08	0.0596	0.0024	0.5959	0.0225	0.0726	0.0013	0.46	451.9	7.5	587.3	86
		#18-1	39.8	296.1	262	1.13	0.36	0.0638	0.0011	0.9253	0.0142	0.1052	0.0011	0.66	644.9	6.2	735.7	36
		#19-1, r	7.7	48.9	512	0.10	0.19	0.0518	0.0061	0.0227	0.0025	0.0032	0.0001	0.34	20.4	0.8	278.4	251
		#20-1	45.9	181.1	1018	0.18	0.07	0.0526	0.0013	0.3527	0.0077	0.0487	0.0006	0.52	306.5	3.4	310.3	54
		#21-1	88.1	98.5	1591	0.06	0.03	0.0622	0.0038	0.0501	0.0028	0.0059	0.0001	0.43	37.6	0.9	681.0	124
		#22-1	1.6	11.2	64	0.18	0.14	0.0555	0.0062	0.0390	0.0041	0.0051	0.0002	0.35	32.9	1.2	430.8	230
		#23-1	76.8	1495.3	251	5.96	2.27	0.0598	0.0019	0.8719	0.0254	0.1058	0.0015	0.50	648.1	8.9	597.4	67
		#24-1, c	32.5	54.6	683	0.08	0.03	0.0574	0.0015	0.5981	0.0145	0.0756	0.0010	0.52	470.0	5.7	506.9	57
		#25-2, r	33.6	41.4	488	0.08	0.03	0.0568	0.0012	0.5573	0.0104	0.0712	0.0008	0.58	443.4	4.6	484.2	45
Classification	Mafic–ultramafic	#1-1	9.2	154.4	161	0.96	0.34	0.0542	0.0026	0.3591	0.0163	0.0481	0.0008	0.39	302.7	5.2	378	103
Lithology	Amphibolite	#2-1	4.4	82.3	68	1.21	0.46	0.0543	0.0084	0.3542	0.0528	0.0473	0.0022	0.31	298.1	13.6	383	316
Sample	VN26	#3-1	7.4	149.6	115	1.30	0.47	0.0544	0.0025	0.3570	0.0158	0.0476	0.0008	0.37	299.7	4.8	389	101
		#4-1	6.0	136.8	106	1.29	0.48	0.0535	0.0046	0.3401	0.0280	0.0461	0.0012	0.31	290.8	7.2	349	182
		#5-1	4.5	67.2	84	0.80	0.26	0.0529	0.0032	0.3492	0.0203	0.0479	0.0010	0.36	301.4	6.1	325	132
		#6-1	15.2	397.9	245	1.62	0.50	0.0531	0.0021	0.3398	0.0124	0.0464	0.0007	0.41	292.5	4.3	334	85
		#7-1	14.8	385.8	244	1.58	0.50	0.0529	0.0021	0.3332	0.0125	0.0457	0.0007	0.41	288.2	4.3	323	88
		#8-1	9.1	195.1	157	1.25	0.38	0.0528	0.0027	0.3432	0.0167	0.0471	0.0009	0.37	296.8	5.2	322	112
		#9-1	66.9	2207.4	954	2.31	0.70	0.0529	0.0011	0.3428	0.0066	0.0470	0.0005	0.57	296.0	3.2	326	46
		#10-1	4.1	66.3	79	0.84	0.27	0.0537	0.0055	0.3428	0.0341	0.0463	0.0014	0.30	291.9	8.5	358	218
		#11-1	7.8	169.0	145	1.16	0.36	0.0576	0.0031	0.3520	0.0177	0.0444	0.0009	0.38	279.8	5.3	513	113
		#12-1	57.1	1820.0	728	2.50	0.79	0.0522	0.0011	0.3401	0.0065	0.0473	0.0005	0.56	298.0	3.2	292	47
		#13-1	6.8	115.0	120	0.96	0.31	0.0500	0.0029	0.3267	0.0180	0.0474	0.0008	0.31	298.8	5.1	194	128
		#14-1, r	28.4	745.6	435	1.71	0.53	0.0508	0.0013	0.3320	0.0079	0.0474	0.0006	0.49	298.4	3.4	234	58
		#14-2, c	22.8	623.2	338	1.85	0.59	0.0513	0.0016	0.3328	0.0095	0.0471	0.0006	0.45	296.4	3.7	255	68
		#15-1	13.6	310.6	223	1.39	0.45	0.0493	0.0019	0.3185	0.0116	0.0469	0.0006	0.37	295.2	3.9	161	88
		#16-1	7.0	133.8	143	0.93	0.31	0.0531	0.0027	0.3026	0.0143	0.0414	0.0007	0.36	261.3	4.3	331	109
		#17-1	3.2	68.9	105	0.65	0.08	0.0522	0.0042	0.2296	0.0178	0.0319	0.0007	0.28	202.4	4.3	294	173
		#18-1	10.2	236.5	175	1.35	0.42	0.0523	0.0022	0.3341	0.0132	0.0463	0.0007	0.38	291.7	4.3	300	93
		#19-1	6.2	149.6	108	1.38	0.45	0.0546	0.0031	0.3358	0.0180	0.0446	0.0008	0.35	281.1	5.1	397	122
		#20-1	5.5	103.6	95	1.10	0.37	0.0519	0.0033	0.3383	0.0202	0.0472	0.0010	0.35	297.5	6.1	283	138
		#21-1	20.0	426.8	389	1.10	0.34	0.0558	0.0016	0.3388	0.0090	0.0441	0.0005	0.46	278.0	3.3	443	63
		#22-1	26.5	757.8	439	1.73	0.53	0.0521	0.0013	0.3284	0.0076	0.0457	0.0005	0.48	288.2	3.1	290	57
		#23-1	35.7	846.5	593	1.43	0.45	0.0519	0.0009	0.3395	0.0053	0.0475	0.0004	0.58	298.9	2.7	281	40
		#24-1	8.9	175.1	160	1.09	0.36	0.0529	0.0019	0.3440	0.0113	0.0472	0.0006	0.39	297.2	3.8	324	78
		#25-1	16.7	426.7	289	1.47	0.45	0.0504	0.0016	0.3270	0.0100	0.0471	0.0006	0.41	296.4	3.6	215	74
		#25-2	16.3	318.1	298	1.07	0.33	0.0518	0.0013	0.3378	0.0078	0.0473	0.0005	0.47	298.2	3.2	276	56

Table 3
Summary of $^{40}Ar/^{39}Ar$ IR-CO_2 laser ages obtained in this study on amphibole, biotite, and white mica.

Sample	Total fusion	2	Weighted plateau	2	$\%^{39}Ar$	Inverse isochron	2	$^{40}Ar/^{36}Ar$	2	MSWD
VN21 biotite	17.03	0.1	17.39	0.11	65	17.02	0.19	377.35	37	1.1
VN21 muscovite	17.24	0.09	17.05	0.09	87	16.94	0.12	303.02	6	0.9
VN24d muscovite	17.03	0.44	16.61	0.35	91	16.45	0.52	306.98	27	0.3
VN25b muscovite	16.98	0.09	16.98	0.09	97	17.02	0.13	291.91	9	0.2
VN24b biotite	11.93	0.26	14.12	0.15	29	14.29	1.88	290.85	55	2.4
VN24b muscovite	16.97	0.07	16.95	0.07	98	16.91	0.08	302.99	9	0.4
VN14a amphibole	18.99	0.72	18.03	0.24	94	17.79	0.37	305.19	11	0.8
VN16d amphibole	21.24	0.21	18.72	0.26	61	18.18	0.57	391.80	94	1.1
VN26 amphibole	22.46	2.05	20.78	0.87	91	20.29	1.8	298.21	8	1.9

MSWD = 1.5). This age is tentatively taken as our best estimate for emplacement and crystallization of the granitic magma. The discordance observed for the other analyses is related either to the metamorphic event, whose age is likely to be similar to that dated by the zircon overgrowths observed in the neighbouring micaschist VN25b, or to an analytical mixing between magmatic and metamorphic isotopic compositions. This age indicates that the sedimentary succession represented by the micaschist VN25b and intruded by the granitic magma was deposited before 280 Ma.

5.1.3. Micaschist VN25b

The micaschist VN25b displays prismatic subhedral to rounded zircon grains. In some cases the rounded shape of the grains is clearly associated with a thin structureless overgrowth, while in other cases no overgrowth was observed and rounding was thus likely acquired during transport of the detritus. Zircon grains analysed display a wide range of ages, in agreement with their detrital origin. The youngest batch of analyses is constituted by zircons with ages ranging from 307 to 325 Ma (n = 3; Fig. 8c), which is broadly comparable to the main age group observed in the diatexite VN21. The age spectrum of detrital zircons also includes a series of concordant grains (n = 4) with ages ranging from 440 to 530 Ma. Two concordant grains have ages of 648 ± 18 and 725 ± 14 Ma. The oldest grains analysed have ages around 1 Ga (apparent $^{206}Pb/^{238}U$ ages of 909 ± 17 and 918 ± 15 Ma). The youngest concordant grain is dated at 307 ± 7 Ma (2), which is a maximum age for deposition of the detritus. Analyses of the overgrowths yield significantly younger ages and plot concordantly at around 20 Ma. Four analyses out of six provide a $^{206}Pb/^{238}U$ weighted mean age of 17.65 ± 0.46 Ma (n = 4, MSWD = 0.8) (Table 2). Two analyses are slightly older at 20.5 ± 1.1 Ma. Although the later age could be biased by a detrital component in the analyses, it is noteworthy that it is consistent with the age of the metamorphic overgrowths in the diatexite VN21 (20.85 ± 0.34 Ma). In addition the age of the main overgrowth in the micaschist is also consistent with the age of one overgrowth analysis (17.80 ± 0.84 Ma) in the diatexite. This suggests that the two ages at around 21 and 18 Ma correspond to two distinct metamorphic events.

5.1.4. Amphibolite lens VN26

Zircons from the amphibolite lens are translucent colourless and display irregular shapes. Twenty-five analyses yield moderate to high Th/U ratios (0.65–2.50, with a mean of 1.33) typical of late-crystallized magmatic minerals as is expected for zircon in mafic magmas. Most of the 27 analysed grains plot concordantly at about 300 Ma, whereas some analyses spread down to c. 200 Ma suggesting various degrees of Pb losses. All analyses plot on a well-defined discordia with an upper intercept age of 295.1 ± 9.2 Ma and a lower intercept, which although the result of a large extrapolation, is zero within errors (972 ± 500 Ma; MSWD = 0.8, Fig. 8d). The former is consistent with the $^{206}Pb/^{238}U$ weighted mean age of the 24 most concordant analyses, which yields an age of 295.2 ± 2.2 Ma (MSWD = 1.5). This age is interpreted as the crystallization of the mafic magma.

5.2. Ar–Ar geochronology

Table 3 and Fig. 9 summarize plateau (Fleck et al., 1977) and inverse isochron ages (Roddick et al., 1980) obtained for the various studied samples (a detailed description of ages and the corresponding table are available in Supplementary Material 4).

5.2.1. Biotite

Biotite from the diatexite VN21 (see Fig. 1), yields a plateau age of 17.39 ± 0.11 Ma in accordance with the inverse isochron age of 17.02 ± 0.19 Ma (Fig. 9a and b). Biotite from the micaschist VN24b (Fig. 9i and j) is unreliable due to chloritization effects (e.g. Di Vincenzo et al., 2003).

5.2.2. Muscovite

Muscovite ages are overall homogeneous with plateau ages ranging from 16.61 ± 0.35 to 17.05 ± 0.09 Ma and inverse isochron ages ranging from 16.45 ± 0.52 to 16.94 ± 0.12 Ma (see Fig. 9c–h, k and l). No significant difference has been detected between the different localities in agreement with a previous study (Monié et al., 1992). It is noteworthy that the biotite age from the diatexite VN21, is older than those obtained on all the studied muscovites (Table 3). This could be related to a size effect (e.g. Dodson, 1973).

5.2.3. Amphibole

Amphiboles display plateau ages ranging from 18.03 ± 0.24 to 20.78 ± 0.87 Ma and inverse isochron ages ranging from 17.79 ± 0.37 and 20.29 ± 0.57 Ma (see Table 3 and Fig. 9m–r). The degasing patterns show an excess of argon for the first steps (Fig. 9m, o and q), which is assumed to occur at the grain margins (e.g. Harrison and McDougall, 1980). The variations of ages detected among the amphiboles can be explained by the compositional differences of the studied amphiboles (e.g. Di Vincenzo and Palmeri, 2001).

6. Sr, Nd, Pb and Hf isotopes

Argon and U–Pb geochronology indicates two main groups of ages. U–Pb ages for some igneous samples cluster around ~280–300 Ma, which we relate to the age of the protoliths for this type of sample. Younger ages at ~ 17–21 Ma are superimposed to the age of magmatic emplacement and are also registered by metamorphic assemblages in some felsic and basic rocks and in the sediments (U–Pb, Ar–Ar and Sm–Nd). Considering that for some rock-types the protolith age is unknown, we decided to correct the isotopic results below for in situ decay using a Miocene age (20 Ma) considering it is the last event registered by all lithologies. However, it is noteworthy that the main conclusions brought by the geochemical analyses of our study remain valid whatever

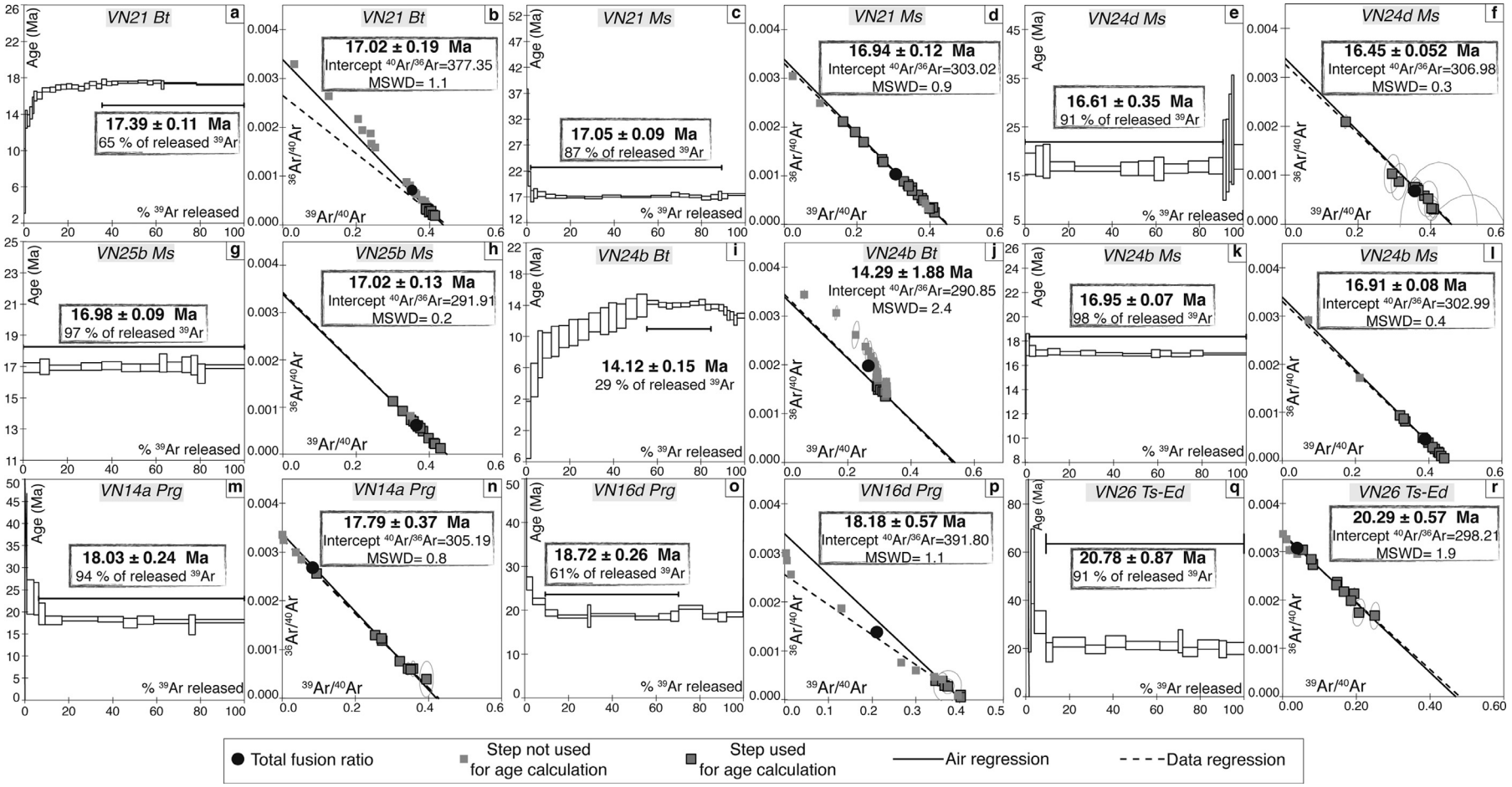

Fig. 9. ^{39}Ar–^{40}Ar plateau and inverse isochron ages on separated micas (biotite and muscovite) and amphiboles with error margin indicated at ±2 . Bt: Biotite; Ms: Muscovite; Prg: Pargasite; Ts-Ed: tschermakite/edenite.

the age correction (20 or 300 Ma) (see the comparative figure in Supplementary Material 5).

6.1. Sr, Nd, Hf and Pb isotopes

Felsic: Both samples (orthogneiss and diatexite) yield low and very close age-corrected Nd isotopic values (0.51219 and 0.51223, respectively) combined to highly radiogenic Sr initial isotopic ratios ($^{87}Sr/^{86}Sr_i > 0.723$; Table 4) and low «Hf$_i$ values (– 2.0 and –5.7, respectively; Table 4). These Sr–Nd–Hf isotopic signatures are close to the average continental crust composition (Rudnick and Goldstein, 1990; Goldstein and Jacobsen, 1988) and, in the Sr–Nd correlation diagram, they partly overlap the domain defined for high-grade sediments from the Alboran Sea (Fig. 10a and b). The Pb–Pb isotopic ratios plot in the field of the upper continental crust or sediments (Fig. 10c). Nd model ages yield values of 1585 and 1990 Ma for the diatexite VN21 and for the orthogneiss VN24d respectively.

Sediments: Only micaschists VN24b and VN25b were analysed for Pb, Sr, Nd and Hf isotopes. Both samples show highly radiogenic $^{87}Sr/^{86}Sr_i$ ratios (0.724665 and 0.754512 respectively) combined to very low Nd initial isotopic composition ($^{143}Nd/^{144}Nd_i = 0.502004$ and 0.502006 respectively) (Fig. 10a and Table 4). The Hf isotope composition has been measured only for sample VN24b and yields a $^{176}Hf/^{177}Hf_i$ value of 0.282686. These isotopic signatures indicate that detritus derived mainly from continental crust material (Vervoort and Patchett, 1996; Vervoort et al., 2000). The calculated Nd T_{DM} model ages of 1701 and 1609 Ma (Table 4) for VN24b and VN25b respectively, suggest that the crustal material is dominated by Mesoproterozoic/Paleoproterozoic source rocks. The Pb isotopic compositions yield highly radiogenic Pb isotopic ratios typical of upper crustal material (Table 4 and Fig. 10c).

Mafic and ultramafic samples: The two ultramafic rocks VN32a and VN24a show significantly different isotopic signatures. Sample VN24a displays high radiogenic Nd and Hf initial values (0.513116 and 0.283129, respectively) typical of mantle-derived rocks (Fig. 10b). In contrast, this sample yields a radiogenic Sr isotopic ratio (0.70975, Table 4) unusual for a typical mantle-derived rock even if seawater alteration cannot be ruled out. Such a radiogenic Sr ratio is correlated with the high loss on ignition measured for this rock (>14%). Sample VN32a yields Sr, Nd, Hf and Pb isotopic ratios very distinct from those characterizing sample VN24a but also significantly different from unmodified mantle-derived rocks. In the four isotopic systems, the isotopic values show a good correlation and plot in intermediate position between the depleted mantle reservoir and the continental crust component (Fig. 10a–c). Similar intermediate isotopic signatures have been previously obtained for mafic or ultramafic rocks, for example for Cr-rich websterites from the Ronda massif. This signature can be attributed to in situ melting of material with crustal related geochemical signatures (i.e. sediments) or imparted to the mantle by fluids/melts issuing from a subducting slab (Marchesi et al., 2012).

In the case of the amphibolite lens VN26, whole-rock and coexisting amphibole and feldspar have been analysed (Table 4). Nd, Sr and Pb isotopic values for minerals and WR define a very limited range of variation, from 0.51241 to 0.51242, from 0.70890 to 0.70903 and from 18.489 to 18.515 for $^{143}Nd/^{144}Nd$, $^{87}Sr/^{86}Sr$ and $^{206}Pb/^{204}Pb$ ratios, respectively (Table 4). The Hf isotope ratios are homogeneous for the WR and amphibole (i.e. $0.28282 < ^{176}Hf/^{177}Hf_i < 0.28285$). On the Nd–Sr and Hf–Nd isotopic diagrams (Fig. 10a–c), VN26 WR and coexisting minerals plot in an intermediate position between the depleted mantle and a more evolved component similar to the continental crust and/or to a sedimentary component. Reported in a Sm/Nd isochron diagram (Fig. 11), WR and coexisting minerals (amphibole and feldspar) define an isochron with a slope

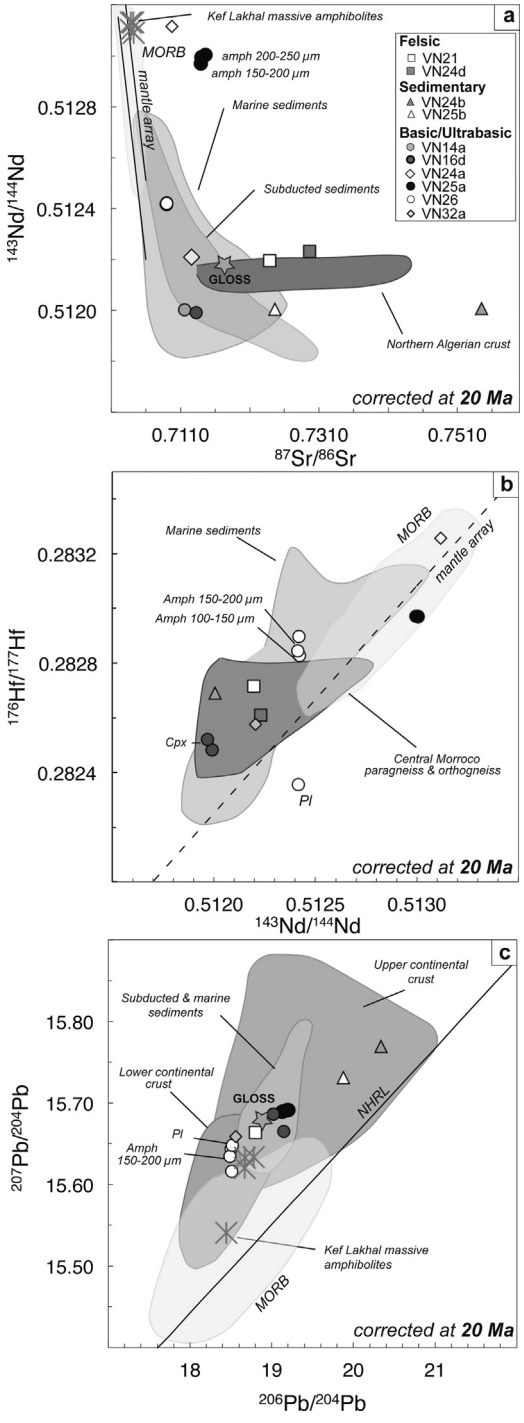

Fig. 10. Sr–Nd–Hf–Pb isotopic diagrams for felsic, sedimentary, mafic and ultramafic samples corrected at 20 Ma. (a) $^{143}Nd/^{144}Nd$ vs $^{87}Sr/^{86}Sr$ plot. Reported for comparison: marine sediments (Ben Othman et al., 1989; Jolly et al., 2006; Vervoort et al., 2011), subducted sediments (Plank and Langmuir, 1998), Northern Algerian crust domain (Fourcade et al., 2001), Kef Lakhal amphibolites (Bosch et al., 2014). (b) $^{176}Hf/^{177}Hf$ vs $^{143}Nd/^{144}Nd$ plot. Reported for comparison: subducted sediments (Vervoort et al., 2011), paragneiss and orthogneiss from central Morocco (Le Fèvre, 2002). (c) $^{207}Pb/^{204}Pb$ vs $^{206}Pb/^{204}Pb$ plot. Reported for comparison: marine and subducted sediments (Ben Othman et al., 1989; Plank and Langmuir, 1998; Vervoort et al., 2011). The Upper Continental Crust (UCC) and the Lower Continental Crust (LCC) fields are from http://georoc.mpch-mainz.gwdg.de/georoc/, Rudnick and Goldstein (1990), Millot et al. (2004) and Chauvel et al. (2014). MORB field is from Georoc database http://georoc.mpch-mainz.gwdg.de/georoc/. Kef Lakhal amphibolites are from Bosch et al. (2014), black stars are Cr-rich pyroxenites from Marchesi et al. (2012).

Table 4

Sr, Nd, Pb and Hf isotopic compositions for whole-rocks and separated minerals from rocks of the footwall of the Kef Lakhal complex (Edough massif, NE Algeria). Uncertainties (±2) refer to within-run precision, given as standard error on the mean (SE) quoted at the 95% confidence level. Analytical errors on Pb isotopic ratios are better than 250 ppm. Rb, Sr, Sm, Nd, Lu, Hf, U, Th and Pb concentrations (ppm) were measured by ICP-MS with precision estimated to ±1%. «Sr, «Nd, «Hf values were calculated as the deviation from a chondritic uniform reservoir (CHUR) with present-day $^{86}Sr/^{87}Sr = 0.70448$; $^{87}Rb/^{85}Rb = 0.0816$; $^{143}Nd/^{144}Nd = 0.512638$; $^{147}Sm/^{144}Nd = 0.1966$; $^{176}Hf/^{177}Hf = 0.282772$; $^{176}Lu/^{177}Hf = 0.0332$ (Blichert-Toft and Albarède, 1997; Jacobsen and Wasserburg, 1980). Sm-Nd depleted-mantle model ages (T_{DM}) calculated following DePaolo (1981). –: not analysed. Initial isotopic ratios have been calculated at 20 Ma.

Classification	Felsic rocks		Metasediments	
Lithology	Diatexite	Orthogneiss	Micaschist	Micaschist
Sample	VN21	VN24d	VN24b	VN25b
Type	WR	WR	WR	WR
$^{87}Rb/^{86}Sr$	2.88	4.60	19.05	23.27
$^{87}Sr/^{86}Sr$ (±2)	0.724678 ± 10	0.730977 ± 05	0.759923 ± 09	0.731275 ± 06
Duplicate			*0.760059*	
$^{87}Sr/^{86}Sr_{(i)}$	0.72386	0.72967	0.75451	0.72466
$^{147}Sm/^{144}Nd$	0.13	0.15	0.12	0.12
$^{143}Nd/^{144}Nd$	0.512213 ± 6	0.512252 ± 5	0.512022 ± 5	0.512019 ± 3
$^{143}Nd/^{144}Nd_{(i)}$	0.51220	0.51223	0.51201	0.51200
«$Nd_{(i)}$	−8.2	−7.5	−11.9	−11.9
T_{DM} Nd (Ma)	1585	1990	1701	1609
$^{178}Lu/^{177}Hf$	0.01	0.01	0.01	0.01
$^{176}Hf/^{177}Hf$	0.282715 ± 4	0.282609 ± 3	0.282690 ± 3	–
«$Hf_{(i)}$	−2.0	−5.8	−2.9	–
$^{176}Hf/^{177}Hf_{(i)}$	0.28271	0.28260	0.28269	–
$^{206}Pb/^{204}Pb$	18.8307	19.5172	20.4693	20.0202
$^{207}Pb/^{204}Pb$	15.6652	15.6981	15.7756	15.7380
$^{208}Pb/^{204}Pb$	38.9259	39.0330	40.7592	40.3462
$^{206}Pb/^{204}Pb_{(i)}$	18.803	19.473	20.334	19.878
$^{207}Pb/^{204}Pb_{(i)}$	15.664	15.696	15.769	15.731
$^{208}Pb/^{204}Pb_{(i)}$	38.881	38.981	40.595	40.145

Classification	Mafic–ultramafic rocks													
Lithology	Amphibolite	Amphibolite			Amphibolite				Aarnet amphibolite				Peridotite	Peridotite
Sample	VN14a	VN16d			VN25a				VN26				VN24a	VN32a
Type	WR	WR	cpx	fsp	WR	amph 150–200 mm	amph 200–250 mm	fsp	WR	amph 100–150 mm	amph 150–200 mm	fsp	WR	WR
$^{87}Rb/^{86}Sr$	0.15	0.10	0.04	0.31	0.25	0.87	1.66	0.15	0.19	0.08	0.08	0.36	0.05	0.61
$^{87}Sr/^{86}Sr$ (±2)	0.711594 ± 04	0.713261 ± 07	–	0.712591 ± 05	0.714706 ± 03	0.714358 ± 11	0.714453 ± 07	–	0.709062 ± 03	0.709011 ± 05	0.709051 ± 04	0.708935 ± 08	0.709767 ± 32	0.712860 ± 03
Duplicate					*0.714711 ± 10*				*0.709060 ± 07*					
$^{87}Sr/^{86}Sr_{(i)}$	0.71155	0.71323	–	0.71259	0.71464	0.71411	0.71398	–	0.70901	0.70899	0.70903	0.70883	0.70975	0.71269
$^{147}Sm/^{144}Nd$	0.12	0.20	0.31	0.11	0.21	0.37	0.31	0.11	0.14	0.24	0.20	0.07	0.18	0.17
$^{143}Nd/^{144}Nd$	0.512018 ± 5	0.512017 ± 4	0.512009 ± 6	0.512035 ± 3	0.513032 ± 3	0.513011 ± 5	0.513037 ± 4	0.513033 ± 5	0.512439 ± 4	0.512450 ± 5	0.512443 ± 5	0.512425 ± 5	0.513139 ± 4	0.512226 ± 3
$^{143}Nd/^{144}Nd_{(i)}$	0.51200	0.51199	0.51197	0.51202	0.51300	0.51296	0.51300	0.51302	0.51242	0.51242	0.51244	0.51243	0.51312	0.51220
«$Nd_{(i)}$	−11.9	−12.2	−12.6	−11.6	7.6	6.8	7.5	7.9	−3.8	−3.8	−3.9	−3.9	9.8	−8.0
T_{DM} Nd (Ma)	–	–	–	–	–	–	–	–	–	–	–	–	–	–
$^{178}Lu/^{177}Hf$	0.01	0.02	0.02	0.12	0.02	0.10	0.08	–	0.13	0.01	0.10	0.12	0.38	0.04
$^{176}Hf/^{177}Hf$	–	0.282482 ± 7	0.282520 ± 2	0.282071 ± 8	0.282972 ± 4	–	0.282972 ± 1	0.282970 ± 6	0.282898 ± 5	0.282828 ± 3	0.282845 ± 2	0.282355 ± 4	0.283256 ± 5	0.282576 ± 6
«$Hf_{(i)}$	–	−10.3	−8.9	−24.8	7.1	–	7.0	7.0	4.4	2.0	2.6	−14.7	17.1	−6.9
$^{176}Hf/^{177}Hf_{(i)}$	–	0.28247	0.28251	0.28202	0.28296	–	0.28295	0.28294	0.28285	0.28283	0.28281	0.28231	0.28312	0.28256
$^{206}Pb/^{204}Pb$	19.1218	19.1661	19.0255	19.1544	19.1916	19.2152	19.2240	19.1501	18.5177	18.5075	18.4964	18.5149	–	18.5795
$^{207}Pb/^{204}Pb$	15.6907	15.6662	15.6871	15.6975	15.6924	15.6923	15.6921	15.6902	15.6169	15.6444	15.6350	15.6483	–	15.6598
$^{208}Pb/^{204}Pb$	39.1225	39.2531	39.0781	39.1303	39.2023	39.2020	39.2042	39.1904	38.8149	38.8368	38.8124	38.7888	–	38.6387
$^{206}Pb/^{204}Pb_{(i)}$	19.022	19.147	19.021	19.154	19.124	19.192	19.199	19.150	18.509	18.501	18.487	18.515	–	18.559
$^{207}Pb/^{204}Pb_{(i)}$	15.686	15.665	15.687	15.698	15.689	15.691	15.691	15.690	15.616	15.644	15.635	15.648	–	15.659
$^{208}Pb/^{204}Pb_{(i)}$	39.031	39.242	39.078	39.130	39.192	39.202	39.204	39.190	38.783	38.835	38.810	38.789	–	38.625

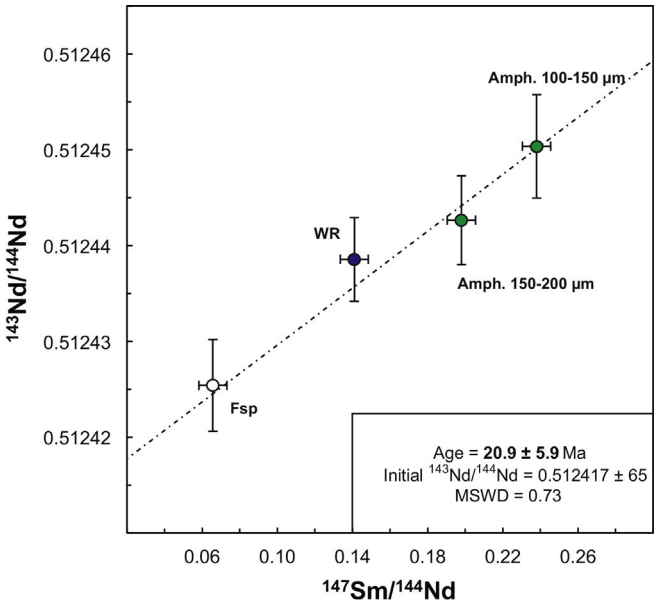

Fig. 11. Sm–Nd isochron diagram for the whole-rock (WR) and separated minerals (amphibole and feldspar) from amphibolite VN26. Error crosses are ±2 .

corresponding to an age of 20.9 ± 5.9 Ma (MSWD = 0.73) and an initial $^{143}Nd/^{144}Nd_i = 0.5124171$. Isotopic ratios have been determined on WR, two amphibole and one feldspar fractions from the amphibolite lens VN25a. Overall, the results are significantly different from VN26 (Table 4). Initial Hf and Nd isotopes are correlated and homogeneous, and plot in the domain of mantle-derived rocks ($0.28292 < {}^{176}Hf/^{177}Hf_i < 0.28296$; $0.51297 < {}^{143}Nd/^{144}Nd_i < 0.51300$). Sr isotopes, only determined for amphibole and WR, show highly radiogenic signatures ($0.71389 < {}^{87}Sr/^{86}Sr < 0.71464$), significantly higher than that of a depleted mantle component or seawater. For both WR and coexisting minerals, the Pb isotopic ratios are homogeneous and radiogenic for the $^{207}Pb/^{204}Pb$ and $^{208}Pb/^{204}Pb$ ratios with relatively low to moderate $^{206}Pb/^{204}Pb$ (Fig. 10c). However, the preservation of typical Nd-Hf mantle signatures is at odd with a simple mixing process.

The two leucocratic amphibolites VN14a and VN16d display the same Sr–Nd–Hf–Pb isotopic signatures (Table 4). VN14 (WR) and VN16d (WR, cpx and fedspar) yield radiogenic initial Sr and Pb signatures coupled to low initial Hf and Nd isotopic ratios (Fig. 10a and b).

7. Discussion

The geochemical and geochronological results obtained on sediments and meta-igneous samples from the footwall of the Kef Lakhal oceanic unit bring new insights into the geodynamical setting in which they were formed and on the events that affected them. This participates to our knowledge of rock units now outcropping on the northern margin of Africa and helps pinpointing the main events that took place during the ante-Alpine and Miocene history of the Western Mediterranean basin.

7.1. Mobility of elements during metamorphic event

Determining how and to what extent the different chemical elements will potentially be mobilized during Miocene metamorphism is a necessary step before trying to interpret geochemical data in terms of reservoirs from where they derived. In this section we investigate the behaviour of the major and trace elements, in order to decipher which can be used with confidence and which should be regarded with caution.

The high-grade metamorphic unit consists of a shear zone containing mafic lenses interbedded in sediments. The studied samples are in contact with the overlying Kef Lakhal massive amphibolitic unit, for example in localities 2–3–4 or in contact with the crustal dome in locality 1 (Fig. 1). Shear zones constitute the most favourable zones to channelize fluid flow (e.g. Garofalo, 2012; Menegon et al., 2015). At lower crustal equilibrium conditions, i.e. 6.5–8 kbar and 700–730 °C, close to the metamorphic conditions underwent by the studied samples (Caby et al., 2001), fluid circulation is preferentially localized within relatively brittle meta-intrusives rocks and in veined brecciated and altered zones around their margins and in strongly recrystallized less competent zones (e.g. Oliver et al., 1990; Ague, 2011). In our study, the latter are represented, for example, by the actinote-rich levels similar to those described in Section 4.1. In addition, works on sediments deformed following a ductile stress (e.g. Oliver et al., 1990) have demonstrated that fluid flow is often negligible. Thus, in the absence of developed brittle deformation in the studied samples, we could infer that the mobility of the elements during metamorphism remained limited.

Moreover, the studied diatexite and orthogneiss display feldspars with myrmekite, interpreted as resulting from dynamic recrystallization on high-stress boundary of K-Feldspar (Simpson and Wintsch, 1989; Pryer, 1993) for pressure and temperature lower than 15 kbar and 700 °C, respectively (e.g. Pryer, 1993; Chopin et al., 2012). Conversely to the study of Simpson and Wintsch (1989) and Pryer (1993), the lack of zoning for K, Na and Ca in both myrmekite and associated K-feldspar porphyroclast suggests that only diffusion processes would explain the myrmekite formation (e.g. Menegon et al., 2006).

In the amphibolites no witness of partial melting event, such as melt pockets or mineral gulfs, has been observed in the studied samples. Conversely, in the case of the ultramafic rocks, petrological examinations have shown that late exchanges with strong serpentinization effects and, in the case of sample VN32a, late recrystallization of numerous amphiboles are observed, as described for Oman (e.g. Khedr et al., 2014).

In order to discuss in more details the mobility of elements during the Miocene metamorphism, major elements and inter-elements ratios distribution are compared to UCC, GLOSS and MORB domains (see Fig. 12a–f). In addition, extended trace elements patterns normalized against Upper Continental Crust (UCC, McLennan, 2001) for sediments, diatexite and orthogneiss on one hand, and against E-DMM (Workman and Hart, 2005) for amphibolites and ultrabasic rocks on the other hand are presented (see Fig. 12g–j). The main conclusions provided by these diagrams are the following:

(i) For diatexite, orthogneiss and sediments, the trace elements patterns, except for Sr and Ba (and Pb for sediments), are regular and flat with strong similarities with UCC (sample/UCC ratio close to 1) (Fig. 12g and h). Such trace elements distribution, similar to the UCC, can be attributed to the source characteristics of the studied rocks and not to later disturbances. Similarly, in the diagrams K_2O vs Al_2O_3 and MgO vs Al_2O_3 (Fig. 12b and c) these samples show strong similarities with both UCC and GLOSS suggesting no major gain or loss of these elements during metamorphism. Thus, for these elements it can be considered that the effect of metamorphism was negligible.

(ii) Mobile elements such as Ba, Sr and Pb (the later considered only for sediments) show negative peaks in Fig. 12g and h, and thus clearly differ from the "normal" UCC distribution. This can also be observed in the Fig. 12a, e and f where diatexite,

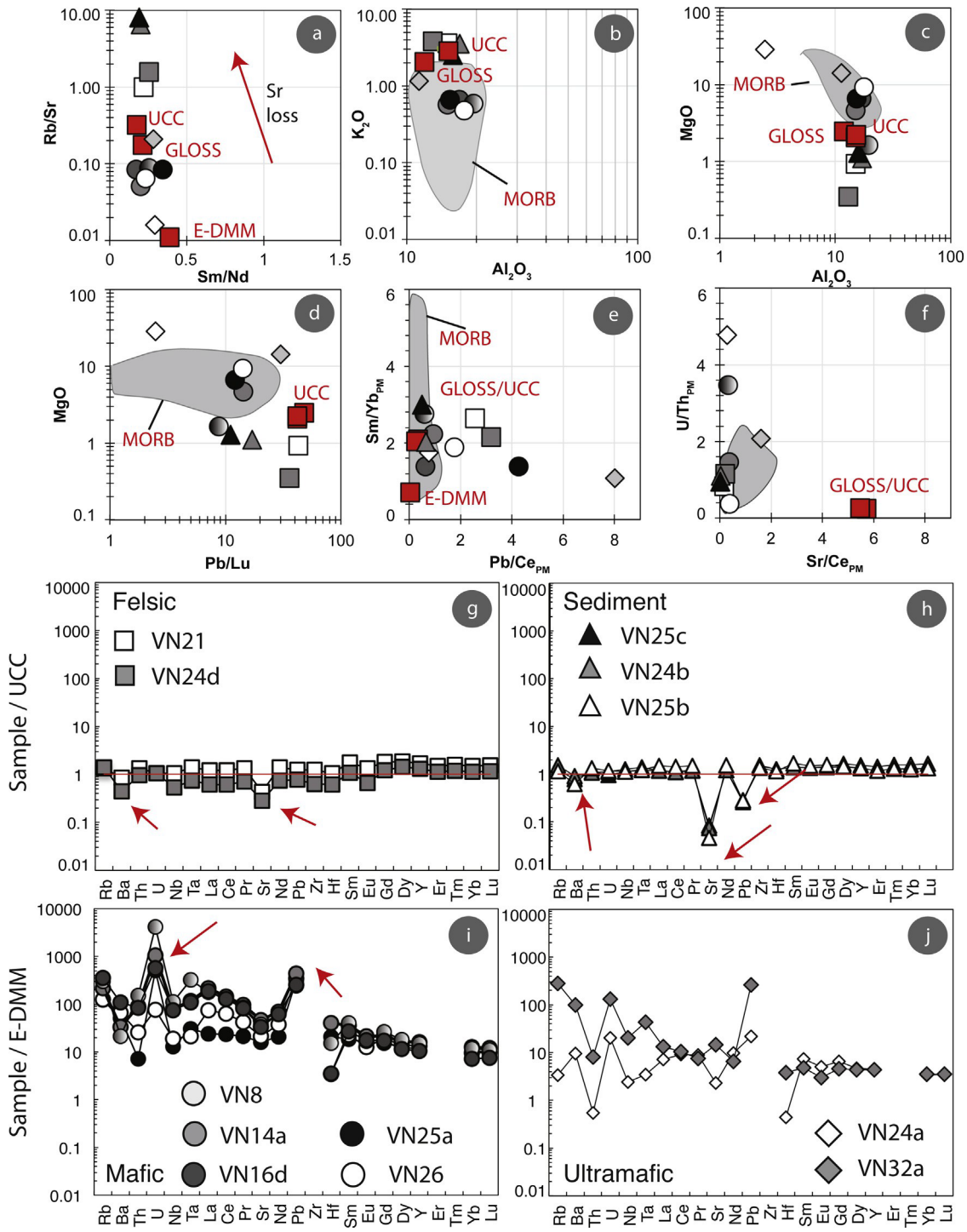

Fig. 12. Diagrams illustrating the mobility of elements during the Miocene metamorphic event. (a–f) Rb/Sr vs Sm/Nd, K_2O vs Al_2O_3, MgO vs Al_2O_3, MgO vs Pb/Lu, Sm/Yb_{PM} vs Pb/Ce_{PM} and U/Th_{PM} vs Sr/Ce_{PM}. GLOSS after Plank and Langmuir, 1998, Upper Continental Crust (UCC) after McLennan (2001) and after Condie (1993), E-DMM after Workman and Hart (2005), MORB from GEOROC database http://georoc.mpch-mainz.gwdg.de/georoc/. (g, h) UCC-normalized trace element diagrams for felsic rocks and sediments. UCC after McLennan (2001). (i, j) E-DMM-normalized trace element diagrams for basic and ultramafic rocks. E-DMM after Workman and Hart (2005).

orthogneiss and sediments clearly differ from both UCC and GLOSS. For example, all samples show moderate (diatexite) to strong (sediments) Rb/Sr enrichment interpreted in agreement with Fig. 12a, g and h as a Sr loss. This observation allows us to propose a loss of these elements, tentatively attributed to the Miocene metamorphism and fluid circulation. Thus, for these lithologies, the use of these elements in the discussion about the sources will only be done with caution.

(iii) In Fig. 12b–d, the amphibolites are located in the MORB domain suggesting no major or only limited perturbation of the major elements composition during metamorphism.

(iv) The PM-normalized patterns of amphibolites (Fig. 5f) became significantly more regular, when normalized to enriched-DMM (Fig. 12i). This suggests that these patterns reflect source characteristics. Only few elements still show marked troughs such as U, Pb, and to a lesser degree Sr.

(v) Negative peaks observed for such reputed mobile elements can be interpreted either as reflecting mobility during metamorphism or as source characteristics. In the later case, U and Pb enrichments could be related to contribution of a subduction-component due to slab dehydration (Miller et al., 1994) or to contamination by a crustal component. This will be discussed in more details in the following paragraphs of the discussion.

(vi) The ultrabasic samples, in particular sample VN24, show very disturbed trace element patterns for both PM- or E-DMM-normalized diagrams. Similarly, they do not overlap the MORB domain, (Fig. 12d–f). Geochemical constraints for these samples should therefore be used with caution.

(vii) At least, it is noteworthy that Hf and Nd isotopes, considered as immobile during fluid circulation, are correlated for the large majority of samples (see Fig. 10) and can thus be used with confidence to discuss the origin of the studied samples.

7.2. *Ante-Alpine history of rocks from the footwall*

Rocks from the footwall display a spatial association of metasediments and metamorphosed felsic and mafic/ultramafic rocks. This association is best portrayed by locality 1 where lenses of amphibolite, interpreted as interbedded magmatic rocks, and metasediments are observed, together with metre-sized boudins of ultramafic rocks (Fig. 2).

In the sediment VN25b the youngest detrital zircon grain analysed points to a deposition age younger than 307 ± 7 Ma. In addition, at this location, the age of the orthogneiss VN24d, intruding the sediments, allows to bracket deposition between 307 ± 7 and 281 ± 4 Ma. This is fully consistent with the age of the amphibolite VN26 interpreted as contemporaneous to the sedimentation and dated at 295.2 ± 2.2 Ma. These ages indicate that the sediments were deposited in the late Carboniferous/early Permian. Such ages are widespread in the Hercynian belt and have been related either to post-orogenic extension driven by gravity collapse of the thickened variscan crust (e.g. Tribuzio et al., 1999; Paquette et al., 2003), or to the incipient stages of extension that led to the Jurassic opening of the Neotethys (Stampfli and Borel, 2002). In northern Africa, it is noteworthy that upper Carboniferous/lower Permian (300–280 Ma) events are known in the Rehamna and Djebilet Massifs of Morocco (Chopin et al., 2014; Hoepffner et al., 2005, 2006; Michard et al., 2010), where they have been interpreted as reflecting the frontal collision between Laurentia and Gondwana (e.g. Chopin et al., 2014). Similar ages associated in some cases with identical lithologies are widespread in the European-paleomargin, for instance in the Mulhacén Complex in the Betics (Puga et al., 2011), or in Calabria (e.g. Festa et al., 2012). In Greater and Lesser Kabylia, which constitute fragments of the Paleo-European margin accreted to Africa during the Cenozoic, Early Permian magmatism and metamorphism (Peucat et al., 1996; Hammor et al., 2006) were interpreted as reflecting the early stages of extensional tectonics that ultimately led to the Neotethys opening, similarly to high-grade granulite facies metamorphism registered in the European lower crust (e.g. Rossi et al., 2006). In the Edough dome, Bruguier et al. (2009) identified a magmatic episode at 308 7 Ma quickly followed by a metamorphic event at 286 ± 11 Ma. These ages are in good agreement with geochronological data presented in this study. Whatever the exact significance of this Permian event, its importance is also emphasized by the occurrence of numerous gabbroic bodies underplated at the base of the thinned continental crust preserved in the Alps and Corsica (e.g. Müntener et al., 2000; Paquette et al., 2003; Schaltegger and Brack, 2007).

The geochemical composition of the sediments can be used to evaluate their provenance and geodynamical setting (e.g. Bhatia, 1983; Bhatia and Crook, 1986; Roser and Korsch, 1988). As discussed in Section 7.1, the mobility of major elements is limited and hence, they can be used in tectonic discriminant diagrams. In the diagram of Bhatia (1983), the sediments plot in the passive margin field (Fig. 13a) suggesting the detritus were mainly derived either from recycled sedimentary and metamorphic rocks of cratonic landmasses, or from granite-gneiss rocks from an uplifted basement. The discriminant function diagram of Roser and Korsch (1988) indicates that source rocks are dominated by quartzose sedimentary rocks, in agreement with recycling of older sediments (Fig. 13b). This is consistent with what is to be expected for passive margin environments. The Zr/Th ratio has been shown to be discriminant between active continental margin and passive margin setting. The three studied sediments display high Zr/Th ratios ranging from 18.2 to 24.6 (see Table 1). These values are very close to those exhibited by metasediments from passive margin settings (19.1 5.8) and contrast with those from active continental margins (9.5 0.7) as proposed by Bhatia and Crook (1986).

Reported in the Pearce et al. (1975) diagram (Fig. 13c), the amphibolite lenses analysed in this study plot in the field of "non-oceanic" amphibolites. Two types of amphibolites have been previously recognized in the Edough massif (Ahmed-Said and Leake, 1992, 1997). Type 1 is made of massive amphibolites

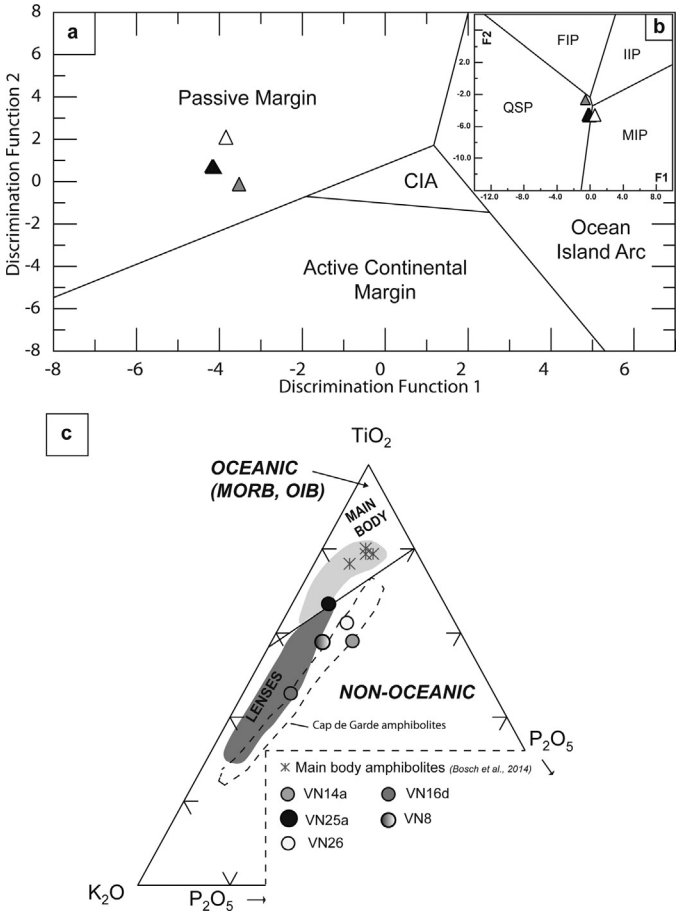

Fig. 13. (a) Discrimination diagram for sedimentary rocks (Bhatia, 1983). CIA: continental island arc. (inset-b) Discrimination diagram for sedimentary rocks (Roser and Korsch, 1988). QSP: Quartzose sedimentary provenance; MIP: Mafic igneous provenance; FIP: felsic igneous provenance, IIP: intermediate igneous provenance. (c) K_2O–TiO_2–P_2O_5 plot after Pearce et al. (1975) for amphibolite lenses analysed in this study. Asterisks and light grey field: Kef Lakhal main body (massive amphibolites) after Bosch et al. (2014) and Ahmed-Said and Leake (1997) respectively; Dark grey field: amphibolite lenses after Ahmed-Said and Leake (1997); Dashed field: amphibolites from the "Cap de Garde" after Hadj-Zobir et al. (2014).

constituting the Kef Lakhal complex. These amphibolites plot in the oceanic domain of Fig. 13c. They have N- to E-MORB affinities (Ahmed-Said and Leake, 1997) and geochemical features (negative spikes in HFS elements) characteristic of a subduction context (Bosch et al., 2014). Type 2 is represented by amphibolite lenses inserted within metapelites overthrust by the Kef Lakhal complex and considered by Ahmed-Said and Leake (1997) to have formed in an island-arc context. Our new data on amphibolite lenses from the footwall display a consistent picture of non-oceanic magmatic material, which combined with the informations given by the associated sediments is also in agreement with a passive margin setting. A possible equivalent to type 2 amphibolites is constituted by amphibolite layers and lenses outcropping in the Cap de Garde area, north of Annaba, which are intercalated within Paleozoic metasediments. However, conversely to amphibolites analysed in this study and to type 2 amphibolites of Ahmed-Said and Leake (1997), they are characterized by a positive Nb–Ta anomaly, which is lacking in our samples, and have been interpreted as within plate alkali-basalts (Hadj-Zobir et al., 2014). In the present light of our knowledge, the relationships between amphibolites from the footwall of the Kef Lakhal complex and the Cap de Garde area are thus still to be investigated.

Taken all together the results of this study indicate that the footwall of the Kef Lakhal complex includes an upper Carboniferous/lower Permian sedimentary sequence with a passive margin affinity. This unit may be para-autochtonous and thus represents the northern passive margin of Gondwana (e.g. Brendan Murphy et al., 2008) or, by similarity with Lesser and Greater Kabylia which display early Permian high-grade metamorphism and magmatism (e.g. Peucat et al., 1996; Hammor et al., 2006), may represent a piece of the paleo-European margin fragmented and accreted to Africa during the opening of the Western Mediterranean.

A further examination of geochronological results from detrital zircons in the micaschist VN25b indicates that the source rocks have a large range of ages (from 300 to 1000 Ma). Although no grain older than 1.0 Ga were found, a contribution from a Mesoproterozoic/Paleoproterozoic or older crustal segment is indicated by the 1.6 Ga Nd T_{DM} model age of this sediment. The later concurs with the Nd T_{DM} age of the neighbouring micaschist VN24b (1.7 Ga) and with those displayed by felsic rocks (Table 4). It is noteworthy that *c.* 1.0 Ga old grains are not known in the Paleoproterozoic West African Craton or in the Neoproterozoic Hoggar Mountains (e.g. Linnemann et al., 2011), which indicates a distal origin or recycling of older sedimentary sequences, at least for part of the sediments. This set apart the age spectrum of detrital zircons, although limited, is dominated by Permo-Carboniferous (300–330 Ma) and Cambro-Ordovician (527 ± 9–443 ± 9 Ma) old grains, with subordinate Pan-African detrital zircons (648 ± 18 and 725 ± 14 Ma). The occurrence of Hercynian zircons, along with the lack of Paleoproterozoic zircons, rules out a provenance from the West African Craton, which may not have been a topographic high at the time of deposition. The age spectrum is more consistent with a western origin (present-day coordinates) of the sediments from the Hercynian belt of Morocco or Iberia (see Linnemann et al., 2004, 2008; El Hadi et al., 2006) or even further west, from Laurentia (in order to take into account the 1.0 Ga old grains), which is placed next to the northwestern border of Gondwana in Carboniferous/Permian times (e.g. Kroner and Romer, 2013). It is noteworthy that the occurrence of high reliefs in this area, as a result of the frontal collision between Laurentia and Gondwana, is consistent with a western origin for the sediments. Lastly, Hercynian as well as Pan-African detrital zircons identified in the metasediments satisfactorily match ages known in the Western Meseta and High Atlas respectively (for a review of ages in this area see Chopin et al., 2014). This area constitutes therefore one of the most plausible source region for the sediments.

7.3. Geochemical features of the mafic rocks and their implications on the mantle sources

Most samples yield results consistent with derivation from a DMM type source reservoir with contribution of a component that has high Pb and Sr but low Nd and Hf isotopic signatures. The latter most likely represents a continental crust component or a component derived form it (sediments). Samples VN24a (ultramafic) and VN25a (amphibolite) display a different behaviour and share with the other mafic/ultramafic samples radiogenic to highly radiogenic Pb and Sr isotopic signatures, significantly higher than any unmodified mantle reservoir, but preserve Nd and Hf signatures typical or close to an unmodified depleted mantle reservoir. For sample VN24a, the measured Sr isotopic signature is too high ($^{87}Sr/^{86}Sr > 0.710$) to be explained by seawater interaction only, and requires participation of a high Sr component or a high Rb component combined with a long-time integration. The observation that Nd and Hf isotopic signatures are still DMM-like is in agreement with modification mostly by fluids (not melts) released from the continental crust or from a sedimentary component. Such a process has been shown to efficiently decouple the behaviour of incompatible elements such as Pb and Sr from that of more immobile elements such as Nd and Hf (Class et al., 2000). Conversely to VN24a and VN25a, most samples with isotopic signatures intermediate between DMM and a crustal component substantiate interaction with melts as previously evidenced in Ronda Cr-rich pyroxenites (e.g. Marchesi et al., 2012).

Since the studied mafic rocks are spatially associated with sediments and felsic rocks, it is important to evaluate the processes responsible of this modified signature. The transfer of the continental crust signature to the studied mafic samples can result from two different processes: (i) contamination during ascent of the mafic magmas upward in the continental crust; (ii) previous old source mixing before partial melting producing the mafic magmas. Crustal contamination during ascent should result in correlated changes in major elements, trace elements and isotopic composition (e.g. SiO_2 vs $^{143}Nd/^{144}Nd$), which are not observed. Similarly, the strong Zr and Hf negative anomaly observed in the mafic samples (see Fig. 5f), and which is lacking in common upper crustal rocks, precludes a thorough contamination by assimilation during their travel path upward in the crust. Reported in the Th/Yb vs Nb/Yb diagram (Fig. 14a), none of the analysed samples plot in the unmodified MORB array, but are displaced upward, suggesting a subduction related environment. The LILE enrichments, positive Pb spikes (related to slab flux) and HFSE (Nb, Ta, Zr, Hf) depletions are consistent with this view and indicate that the mantle source region was modified by a subduction-related component. Reported in the $^{143}Nd/^{144}Nd$ vs Th/Nd diagram (Fig. 14b), all mafic samples, except VN24a yield Th/Nd consistent with modification of the mantle source by melts originating from a continental crust-derived component, most likely sediments. The low Th/Nd ratio combined to high $^{143}Nd/^{144}Nd$ (but high Sr isotopic signature) of sample VN24a substantiates that its mantle source was dominantly contaminated by fluids. To sum up, it is proposed that the studied mafic rocks derived from melting of an old metasomatized mantle and inherited the geochemical characteristics imparted to the mantle by an ancient subduction event as previously described by Chiarenzelli et al. (2010).

7.4. Timing of metamorphism in the footwall of the Kef Lakhal complex

Following Caby et al. (2001), the metamorphic evolution of the footwall of the Kef Lakhal amphibolite complex reflects evidences for a succession of metamorphic conditions. This evolution is characterized by a high-pressure stage with peak pressures ≥12 kbar

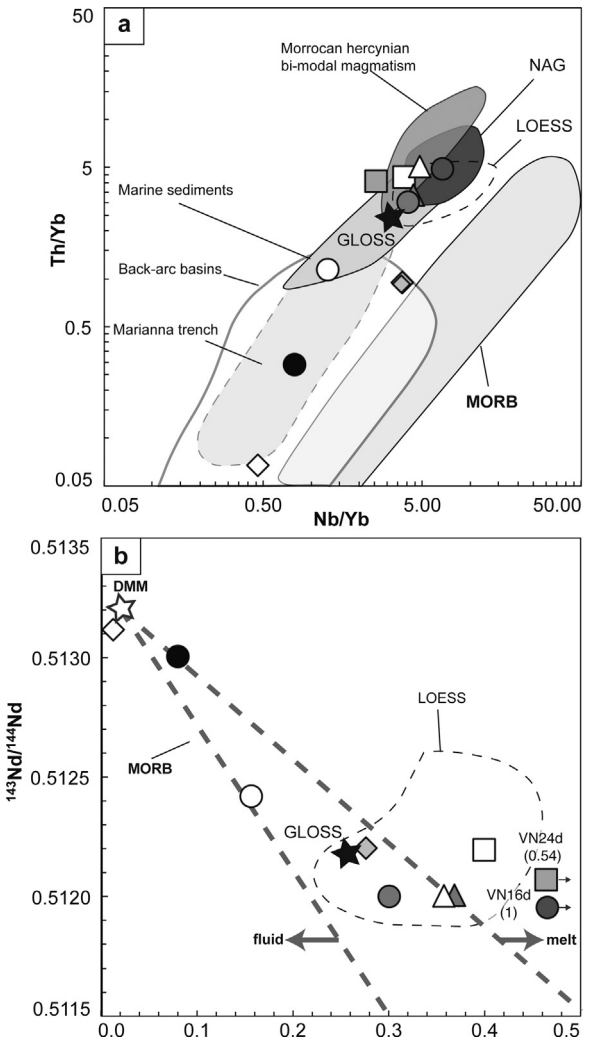

Fig. 14. (a) Th/Yb vs Nb/Yb plot (Pearce and Peate, 1995). Black star is GLOSS after Plank and Langmuir (1998). (b) $^{143}Nd/^{144}Nd$ vs Th/Nd plot for the felsic, sedimentary, mafic and ultramafic rocks. Dashed lines represent vectors connecting the DMM and local sediments after the study of Bosch et al. (2014). LOESS and UCC after Taylor et al. (1983), Taylor and McLennan (1985), Gallet et al. (1998) and Chauvel et al. (2014). Black star is GLOSS after Plank and Langmuir (1998); Morrocan hercynian bi-modal magmatism after Gasquet et al. (1992), marine sediment after Vervoort et al. (2011), NAG is Northern Algerian granitoïds after Fourcade et al. (2001). MORB, Marianna trench and back-arc basin fields are reported from GEOROC database http://georoc.mpch-mainz.gwdg.de/georoc/. DMM from Zindler and Hart (1986). Symbols as in Fig. 10.

for temperatures >740 °C. Recently, UHP diamond-bearing units have also been reported for this area (Caby et al., 2014). Peak pressure conditions were followed by decompression, which was accompanied in the early stages by the production of HP leucosome (Gt, Rt, Ky and antiperthitic plagioclase) reflecting minimum pressure of 8–9 kbar and 650–700 °C. Temperature estimates for the diatexite VN21, close to the contact with the overriding Kef Lakhal complex provide values of 686–727 °C, similar to that provided by the amphibolite VN26 (657–703 °C), close to the eastern contact. The main zircon overgrowths in the diatexite are dated at 20.85 ±0.34 Ma (2). This age is similar to the less precise Sm/Nd age of the metamorphic assemblage in the amphibolite VN26 (20.9± 5.9 Ma; 2) and also to the growth of metamorphic rims around pre-existing detrital zircons in the sediment VN24b (20.5±l .1 Ma; 2). The diatexite VN21 and the amphibolite VN26, both record similar metamorphic temperatures at around 660–730 °C, which we interpret as corresponding to the tectonic emplacement of the hot Kef Lakhal amphibolite complex (Fig. 15a). We thus conclude that the age of 20.85 Ma does not record the climax of HP metamorphism, which was consequently reached before *c.* 21 Ma. Rutile from the amphibolite VN26 yields a slightly but significantly lower temperature of 613 °C. It is difficult to ascribe a precise significance to this temperature since rutile can grow during the prograde stage of metamorphism (e.g. Zheng et al., 2011), but this mineral has also been identified in retrograde quartz-veins postdating HP metamorphism (Chen et al., 2013). The amphibole from VN26 provides an Ar age of 20.8 ± 1.7 Ma (2), which is identical to the age of the main zircon rim in the diatexite. This similarity in age is taken as evidence that cooling down to *c.* 550 °C, the closure temperature of amphibole (Dahl, 1996), occurred within the error margins of both ages and was thus very fast.

This consistent picture of ages at around 21 Ma is disturbed by the main zircon rims in the micaschist VN24b, which provide a younger age of 17.65 ±0.46 Ma (2). This age is reproduced by one discrete rim in the diatexite VN21 (17.8 ±0.9 Ma, 2). The identification of two zircon growth episodes substantiates the occurrence of two distinct metamorphic events. The orthogneiss VN24d, close to the micaschist VN24b, yields a garnet-biotite temperature estimate of 584–621 °C, in good agreement with the Zr-in-rutile temperature of 607 °C for rutile in the same rock. These temperature estimates are in agreement with the *c.* 600 °C temperature for the mylonite bands main activity that assisted most of the low angle, near isothermal uplift of the crust (Caby et al., 2001). A temperature of about 600 °C is thus adopted as our best estimate for the thermal conditions prevailing during this event, the age of which is best dated by the growth of zircon rims in the micaschist at 17.65 ± 0.46 Ma. The temperature for this event (*c.* 600 °C) is within error margins of the amphibole closure temperature (550 ±50 °C after Dahl, 1996). This feature can explain the preservation of a *c.* 21 Ma old age for the VN26 amphibole, along with the younger ages provided by amphiboles from amphibolite VN14a and VN16a (17.75± 0.62 and 18.18± 1.14 Ma respectively; 2). Moreover, this observation indicates that, in the time interval between 21 and 18 Ma, rocks were stored at mid-crustal level, close to 550 °C, a situation that may have been promoted by a blanketing effect related to thrusting of the hot Kef Lakhal Complex. Alternatively, cooling below 550 °C may have occurred between 21 and 18 Ma, and the second event would then be related to reheating of the rocks at a temperature of about 600 °C. Interestingly, the age of this second event is undistinguishable from the age of anatexis of rocks from the core of the Edough dome (17.84 ± 0.12 Ma), which has been related to emplacement of the Sidi Mohamed peridotite into the crustal units (Bruguier et al., 2009). Emplacement of these mantle rocks was interpreted by Caby et al. (2001) to be coeval with the onset of exhumation of the lower crustal units in the core of the Edough Massif and the formation of a metamorphic core complex. The muscovite (weighted mean age of 16.94 ± 0.10 Ma; $n = 4$) and biotite (17.02 ± 0.19 Ma; $n = 1$) ages in this study cluster close to 17 Ma, in agreement with previous results of Monié et al. (1992) on micas from the Edough dome who related these ages to an isothermal decompression of the dome and surrounding units (including the high grade metamorphic unit described in this paper). This indicates that the cooling between 18 and 17 Ma was fast, ≥100 °C/Ma to cool from 550–600 to *c.* 450 °C, the closure temperature of muscovite (e.g. Villa, 1998). In addition, identical muscovite and biotite Ar ages are consistent with an increase in the cooling rate at 17 Ma, and supports an accelerated exhumation as highlighted in Fig. 15b. Such fast cooling features have been also observed in the Betics (Alpujarrides units) and in the Rif (Sebtides units) (Zeck et al., 1992; Monié et al., 1994; Platt and Whitehouse, 1999; Booth-Rea et al., 2003; Michard et al., 2006) where emplacement of peridotite bodies into the crust occurred at 25–20 Ma (e.g. Zindler et al., 1983; Blichert-Toft et al., 1999; Rossetti et al., 2010).

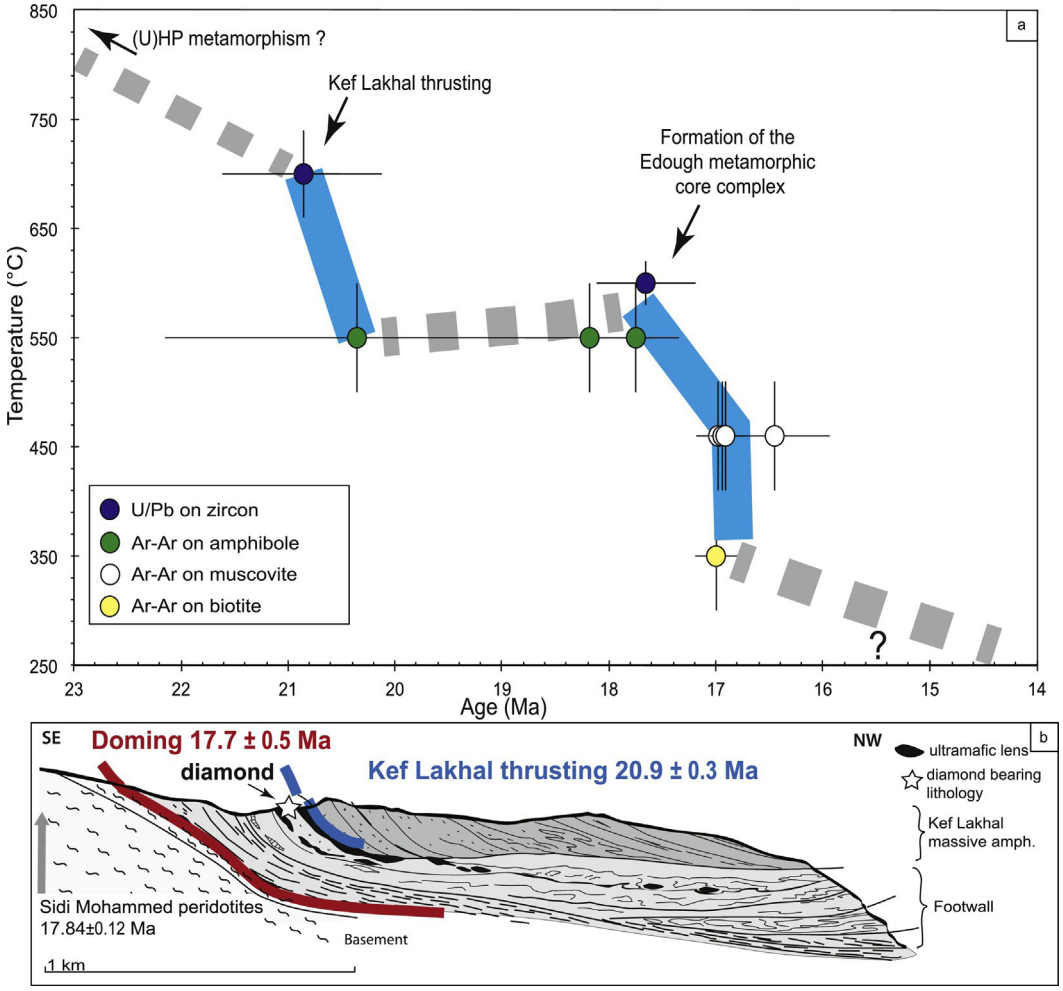

Fig. 15. (a) Time–temperature diagram for the studied samples summarizing U–Pb (zircon) and Ar–Ar (amphibole, muscovite, biotite) ages. (b) Schematic representation of Kef Lakhal and Edough metamorphic pile with the ages of the main events identified in this study (modified after Caby et al., 2001). Closure temperatures are from Dahl (1996) for amphibole, from Hames and Bowring (1994) for muscovite and from Harrison et al. (1985) for biotite. For U–Pb zircon ages, the reported temperatures correspond to: (i) the peak temperature recorded in diatexite VN21 by the garnet-biotite thermometer (Ferry and Spear, 1978; Hodges and Spear, 1982); (ii) the temperatures recorded by the garnet-biotite thermometer (Ferry and Spear, 1978; Hodges and Spear, 1982) in the orthogneiss VN24d and by the Zr-in-rutile thermometry in the micaschist VN25b (Ferry and Watson, 2007) (see text for explanation). Error crosses are ±2 . Occurrence of diamond-bearing lithologies after Caby et al. (2014). Age of Edough doming and emplacement of Sidi Mohammed peridotites after Bruguier et al. (2009).

Thrusting of oceanic fragments onto the continental crust requires a drastic change in the tectonic forces (Agard et al., 2014), that in the case of the Kef Lakhal oceanic unit may be found in tearing or break-off of the retreating Tethyan slab as envisioned in some models (e.g. Maury et al., 2000). Such processes will result from very fast exhumation and in some cases with excision processes (e.g. Johanesen et al., 2014).

8. Conclusion

Rocks from the footwall of the Kef Lakhal complex contain an association of lithologies (sediments, mafic sills and ultramafic boudins) that have geochemical characteristics consistent with a passive margin setting. The sedimentary sequence was deposited between 307 ±7 Ma (the age of the youngest detrital zircon grain analysed) and 281 ±4 Ma (the age of a crosscutting orthogneiss). This time interval for deposition concurs with the age of an interbedded amphibolite lens dated at 295 ±2 Ma. Detrital zircons indicate an origin of the sediments from Pan-African, Hercynian and Cambro-Ordovician rocks, which can be sourced from the Eastern Meseta and High Atlas of Morocco. This supports a North Gondwanan affinity for this sequence rather than a European margin origin. Pb, Sr, Nd and Hf isotopes provide evidence that these Permo-Carboniferous mafic rocks derived from melting of a metasomatized mantle reservoir, which was contaminated by a Paleoproterozoic (or older) sedimentary component recycled into the mantle during a previous subduction event. Geochronological results (U–Pb ages of metamorphic zircon rims, Sm/Nd isochron and Ar–Ar ages on minerals) provide compelling evidences supporting an Alpine age for the HT tectono-metamorphic evolution of rocks from the footwall. These geochronological results indicate that the present-day architecture of the Edough massif is related to two distinct events best dated at 20.85 ±0.34 Ma (2) and 17.65 ±0.46 Ma (2). These two events reflect: (i) thrusting of the oceanic Kef Lakhal complex onto the North African margin at *c.* 21 Ma; (ii) doming and exhumation of the lower crust of the Edough Massif to form a metamorphic core complex at *c.* 18 Ma. Between 18 and 17 Ma, exhumation of the lower crust followed an accelerating rate, with cooling down to 350 °C reached at 17.02 ± 0.19 Ma.

Acknowledgements

The authors are grateful to P. Verdoux, M. Tansu, F. Lecoeur, M. Bonno and P. Telouk for their expertise in TIMS, noble gas MS

and MC-ICP-MS, to C. Nevado and D. Delmas for preparing thin and thick sections, to B. Boyer for assistance during EPMA analyses and to F. Fernandez for SEM imaging. This work is part of the Ph.D. work of L.F. which was supported by a MRT grant. We are grateful to F. Boudier for discussion and help in the thin section examination. Detailed and constructive comments by two anonymous reviewers significantly improved the manuscript. We acknowledge funding by the INSU SYSTER program to D.B. and by the DPGRF France–Algeria collaboration program.

References

Advokaat, E.L., van Hinsbergen, D.J., Maffione, M., Langereis, C.G., Vissers, R.L., Cherchi, A., Schroeder, R., Madani, H., Columbu, S., 2014. Eocene rotation of Sardinia, and the paleogeography of the western Mediterranean region. Earth Planet. Sci. Lett. 401, 183–195.

Agard, P., Zuo, X., Funiciello, F., Ballahsen, N., Faccenna, C., Savva, D., 2014. Obduction: why, how and where. Clues for analog models. Earth Planet. Sci. Lett. 393, 132–145.

Ague, J.J., 2011. Extreme channelization of fluid and the problem of element mobility during Barrovian metamorphism. Am. Mineral. 96, 333–352.

Ahmed-Said, Y., Leake, B.E., 1992. The composition and origin of the Kef Lakhal amphibolites and associated amphibolite and olivine-rich enclaves, Edough, Annaba, NE Algeria. Mineral. Mag. 56, 459.

Ahmed-Said, Y., Leake, B.E., 1997. The petrogenesis of the Edough amphibolites, Annaba, NE Algeria: two unrelated basic magmas and the lherzolite-harzburgite residue of a possible magma source. Mineral. Petrol. 59, 207–237.

Augier, R., Agard, P., Monié, P., Jolivet, L., Robin, C., Booth-Rea, G., 2005. Exhumation, doming and slab retreat in the Betic Cordillera (SE Spain): in situ $^{40}Ar/^{39}Ar$ ages and P–T–d–t paths for the Nevado–Filabride complex. J. Metamorph. Geol. 23, 357–381.

Ben Othman, D.B., White, W.M., Patchett, J., 1989. The geochemistry of marine sediments, island arc magma genesis, and crust-mantle recycling. Earth Planet. Sci. Lett. 94, 1–21.

Bhatia, M.R., 1983. Plate tectonics and geochemical composition of sandstones. J. Geol. 97, 611–627.

Bhatia, M.R., Crook, K.A., 1986. Trace element characteristics of graywackes and tectonic setting discrimination of sedimentary basins. Contrib. Mineral. Petrol. 92, 181–193.

Blichert-Toft, J., Chauvel, C., Albarède, F., 1997. Separation of Hf and Lu for high-precision isotope analysis of rock samples by magnetic sector-multiple collector ICP-MS. Contrib. Mineral. Petrol. 127, 248–260.

Blichert-Toft, J., Albarède, F., 1997. The Lu–Hf isotope geochemistry of chondrites and the evolution of the mantle-crust system. Earth Planet. Sci. Lett. 148, 243–258.

Blichert-Toft, J., Albarede, F., Kornprobst, J., 1999. Lu–Hf isotope systematics of garnet pyroxenites from Beni Bousera, Morocco: implications for basalt origin. Science 283, 1303–1306.

Booth-Rea, G., Azanon, J.M., Garcia-Duenas, V., Augier, R., Sanchez-Gomez, M., 2003. A 'core-complex-like structure' formed by superimposed extension, folding and high-angle normal faulting. The Santi Petri dome (western Betics, Spain). C. R. Geosci. 335, 265–274.

Bosch, D., Bruguier, O., Pidgeon, R.T., 1996. Evolution of an archean metamorphic belt: a conventional and SHRIMP U–Pb study of accessory minerals from the Jimperding metamorphic belt, Yilgarn craton, West Australia. J. Geol. 104, 695–711.

Bosch, D., Garrido, C.J., Bruguier, O., Dhuime, B., Bodinier, J.L., Padròn-Navarta, J.A., Galland, B., 2011. Building an island-arc crustal section: time constraints from a LA-ICP-MS zircon study. Earth Planet. Sci. Lett. 309, 268–279.

Bosch, D., Hammor, D., Mechati, M., Fernandez, L., Bruguier, O., Caby, R., Verdoux, P., 2014. Geochemical study (major, trace elements and Pb–Sr–Nd isotopes) of mantle material obducted onto the North African margin (Edough Massif, North Eastern Algeria): Tethys fragments or lost remnants of the Liguro-Provenc¸al basin? Tectonophysics 626, 53–68.

Bossière, G., Collomb, P., Mahdjoub, Y., 1976. Sur un gisement de péridotite découvert dans le massif de l'Edough (Annaba, Algérie). C. R. Acad. Sci. Paris Sér. II 306, 1039–1045.

Bouillin, J.P., 1986. Le "bassin maghrébin": une ancienne limite entre l'Europe et l'Afrique I' Ouest des AIpes. Bull. Soc. Géol. France 8–11, 547–558.

Brendan Murphy, J., Gutiérrez-Alonso, G., Fernández-Suárez, J., Braid, J.A., 2008. Probing crustal and mantle lithosphere origin through Ordovician volcanic rocks along the Iberian passive margin of Gondwana. Tectonophysics 461, 166–180.

Bruguier, O., Hammor, D., Bosch, D., Caby, R., 2009. Miocene incorporation of peridotite into the Hercynian basement of the Maghrebides (Edough massif, NE Algeria): implications for the geodynamic evolution of the Western Mediterranean. Chem. Geol. 261, 172–184.

Caby, R., Hammor, D., 1992. Le massif de l'Edough (Algérie): Un "Metamorphic Core Complex" d'âge Miocène dans les Maghrébides. C. R. Acad. Sci. Paris Sér. II 314, 829–835.

Caby, R., Hammor, D., Delor, C., 2001. Metamorphic evolution, partial melting and Miocene exhumation of lower crust in the Edough metamorphic core complex, west Mediterranean orogen, eastern Algeria. Tectonophysics 342, 239–273.

Caby, R., Bruguier, O., Fernandez, L., Hammor, D., Bosch, D., Mechati, M., Laouar, R., Ouabadi, A., Abdallah, N., Douchet, C., 2014. Metamorphic diamonds in a garnet megacryst from the Edough Massif (northeastern Algeria). Recognition and geodynamic consequences. Tectonophysics 637, 341–353.

Carminati, E., Wortel, M.J.R., Spakman, W., Sabadini, R., 1998. The role of slab detachment processes in the opening of the western–central Mediterranean basins: some geological and geophysical evidence. Earth Planet. Sci. Lett. 160, 651–665.

Chauvel, C., Blichert-Toft, J., 2001. A hafnium isotope and trace element perspective on melting of the depleted mantle. Earth Planet. Sci. Lett. 190, 137–151.

Chauvel, C., Garc¸on, M., Bureau, S., Besnault, A., Jahn, B.M., Ding, Z., 2014. Constraints from loess on the Hf–Nd isotopic composition of the upper continental crust. Earth Planet. Sci. Lett. 388, 48–58.

Chen, Z.Y., Zhang, L.F., Du, J.X., Lü, Z., 2013. Zr-in-rutile thermometry in eclogite and vein from southwestern Tianshan, China. J. Asian Earth Sci. 63, 70–80.

Chiarenzelli, J., Lupulescu, M., Cousens, B., Thern, E., Coffin, L., Regan, S., 2010. Enriched Grenvillian lithospheric mantle as a consequence of long-lived subduction beneath Laurentia. Geology 38, 151–154.

Chopin, F., Schulmann, K., S˘típská, P., Martelat, J.E., Pitra, P., Lexa, O., Petri, B., 2012. Microstructural and metamorphic evolution of a high-pressure granitic orthogneiss during continental subduction (Orlica–S˘niez˙nik dome, Bohemian Massif). J. Metamorph. Geol. 30, 347–376.

Chopin, F., Corsini, M., Schulmann, K., El Houicha, M., Ghienne, J.F., Edel, J.B., 2014. Tectonic evolution of the Rehamna metamorphic dome (Morocco) in the context of the Alleghanian–Variscan orogeny. Tectonics 33, 1154–1177.

Class, C., Miller, D.M., Goldstein, S.L., Langmuir, C.H., 2000. Distinguishing melt and fluid subduction components in Umnak Volcanics, Aleutian Arc. Geochem. Geophys. Geosyst. 1, 1004, http://dx.doi.org/10.1029/1999GC000010.

Condie, K.C., 1993. Chemical composition and evolution of the upper continental crust: contrasting results from surface samples and shales. Chem. Geol. 104, 1–37.

Connelly, J.N., Ulfbeck, D.G., Thrane, K., Bizzarro, M., Housh, T., 2006. A method for purifying Lu and Hf for analyses by MC-ICP-MS using TODGA resin. Chem. Geol. 233, 126–136.

Dahl, P.S., 1996. The effects of composition on retentivity of argon and oxygen in hornblende and related amphiboles: a field-tested empirical model. Geochim. Cosmochim. Acta 60, 3687–3700.

DePaolo, D.J., 1981. Neodymium isotopes in the Colorado Front Range and implications for crust formation and mantle evolution in the Proterozoic. Nature 291, 193–197.

Dercourt, J.E.A., Zonenshain, L.P., Ricou, L.E., Kazmin, V.G., Le Pichon, X., Knipper, A.L., Grandjacquet, C., Sbortshikov, I.M., Geyssant, J., Lepvrier, C., Pechersky, D.H., Boulin, J., Sibuet, J.C., Savostin, L.A., Sorokhtin, O., Westphal, M., Bazhenov, M.L., Lauer, J.P., Biju-Duval, B., 1986. Geological evolution of the Tethys belt from the Atlantic to the Pamirs since the Lias. Tectonophysics 123, 241–315.

Di Vincenzo, G., Palmeri, R., 2001. An $^{40}Ar–^{39}Ar$ investigation of high-pressure metamorphism and the retrogressive history of mafic eclogites from the Lanterman Range (Antarctica): evidence against a simple temperature control on argon transport in amphibole. Contrib. Mineral. Petrol. 141, 15–35.

Di Vincenzo, G., Viti, C., Rocchi, S., 2003. The effect of chlorite interlayering on $^{40}Ar–^{39}Ar$ biotite dating: an 40Ar–39Ar laser-probe and TEM investigations of variably chloritised biotites. Contrib. Mineral. Petrol. 145, 643–658.

Dodson, M.H., 1973. Closure temperature in cooling geochronological and petrological systems. Contrib. Mineral. Petrol. 40, 259–274.

Doglioni, C., Gueguen, E., Sàbat, F., Fernandez, M., 1997. The western Mediterranean extensional basins and the Alpine orogen. Terra Nova 9, 109–112.

El Hadi, H., Simancas, J.F., Tahiri, A., González-Lodeiro, F., Azor, A., Martínez-Poyatos, D., 2006. Comparative review of the Variscan granitoids of Morocco and Iberia: proposal of a broad zonation. Geodinamica Acta 19, 103–116.

Faccenna, C., Becker, T.W., Lucente, F.P., Jolivet, L., Rossetti, F., 2001. History of subduction and back arc extension in the Central Mediterranean. Geophys. J. Int. 145, 809–820.

Ferry, J.T., Spear, F.S., 1978. Experimental calibration of the partitioning of Fe and Mg between biotite and garnet. Contrib. Mineral. Petrol. 66, 113–117.

Ferry, J.M., Watson, E.B., 2007. New thermodynamic models and revised calibrations for the Ti-in-zircon and Zr-in-rutile thermometers. Contrib. Mineral. Petrol. 154, 429–437.

Festa, V., Fornelli, A., Paglionico, A., Pascazio, A., Piccarreta, G., Spiess, R., 2012. Asynchronous extension of the late-Hercynian crust in Calabria. Tectonophysics 518, 29–43.

Fleck, R.J., Sutter, J.F., Elliot, D.H., 1977. Interpretation of discordant $^{40}Ar/^{39}Ar$ age-spectra of Mesozoic tholeiites from Antarctica. Geochim. Cosmochim. Acta 41, 15–32.

Fleet, M.E., Barnett, R.L., 1978. Al^{iv}/Al^{vi} partitioning in calciferous amphiboles from the Frood Mine, Sudbury, Ontario. Canad. Mineral. 16, 527–532.

Fourcade, S., Capdevila, R., Ouabadi, A., Martineau, F., 2001. The origin and geodynamic significance of the Alpine cordierite-bearing granitoids of

northern Algeria. A combined petrological, mineralogical, geochemical and isotopic (O, H, Sr, Nd) study. Lithos 57, 187–216.
Frizon de Lamotte, D., Andrieux, J., Guezou, J.C., 1991. Cinématique des chevauchements néogenes dans l'Arc betico-rifain; discussion sur les modèles géodynamiques. Bull. Soc. Géol. France 162, 611–626.
Frizon de Lamotte, D., Saint Bezar, B., Bracène, R., Mercier, E., 2000. The two main steps of the Atlas building and geodynamics of the western Mediterranean. Tectonics 19, 740–761.
Gallet, S., Jahn, B.M., Lanoë, B.V.V., Dia, A., Rossello, E., 1998. Loess geochemistry and its implications for particle origin and composition of the upper continental crust. Earth Planet. Sci. Lett. 156, 157–172.
Gao, S., Liu, X., Yuan, H., Hattendorf, B., Günther, D., Chen, L., Hu, S., 2002. Determination of forty two major and trace elements in USGS and NIST SRM glasses by laser ablation-inductively coupled plasma-mass spectrometry. Geostand. Newslett. 26, 181–196.
Garofalo, P.S., 2012. The composition of Alpine marine sediments (Bündnerschiefer Formation, W Alps) and the mobility of their chemical components during orogenic metamorphism. Lithos 128, 55–72.
Gasquet, D., Leterrier, J., Mrini, Z., Vidal, P., 1992. Petrogenesis of the Hercynian Tichka plutonic complex (Western High Atlas, Morocco): trace element and Rb/Sr and Sm/Nd isotopic constraints. Earth Planet. Sci. Lett. 108, 29–44.
Goldstein, S.J., Jacobsen, S.B., 1988. Nd and Sr isotopic systematics of river water suspended material: implications for crustal evolution. Earth Planet. Sci. Lett. 87, 249–265.
Hadj-Zobir, S., Oberhänsli, R., 2013. The Sidi Mohamed peridotites (Edough massif, NE Algeria): evidence for an upper mantle origin. J. Earth Syst. Sci. 122, 1455–1465.
Hadj-Zobir, S., Altenberger, U., Günter, C., 2014. Geochemistry and petrology of metamorphosed submarine basic ashes in the Edough Massif (Cap de Garde, Annaba, northeastern Algeria). C. R. Geosci. 346, 244–254.
Hames, W.E., Bowring, S.A., 1994. An empirical evaluation of the argon diffusion geometry in muscovite. Earth Planet. Sci. Lett. 124, 161–169.
Hammor, D., (Ph.D. thesis) 1992. Du Panafricain au Miocène: 600 millions d'années d'évolution polycyclique dans le massif de l'Edough (Algérie Nord-Orientale) retracés par la pétrologie, la tectonique et la géochronologie (U/Pb, Rb/Sr, Sm/Nd et $^{39}Ar/^{40}Ar$). Université de Montpellier II, pp. 205.
Hammor, D., Bosch, D., Caby, R., Bruguier, O., 2006. A two-stage exhumation of the Variscan crust: U–Pb LA-ICP-MS and Rb–Sr ages from Greater Kabylia, Maghrebides. Terra Nova 18, 299–307.
Harrison, T.M., McDougall, I., 1980. Investigations of an intrusive contact, northwest Nelson, New Zealand—II. Diffusion of radiogenic and excess 40 Ar in hornblende revealed by 40Ar39Ar age spectrum analysis. Geochim. Cosmochim. Acta 44, 2005–2020.
Harrison, T.M., Duncan, I., McDougall, I., 1985. Diffusion of ^{40}Ar in biotite: temperature, pressure and compositional effects. Geochim. Cosmochim. Acta 49, 2461–2468.
Herron, M.M., 1988. Geochemical classification of terrigenous sands and shales from core or log data. J. Sediment. Petrol. 58, 820–829.
Hodges, K.V., Spear, F.S., 1982. Geothermometry, geobarometry garnet closure temperatures and the Al_2SiO_5 triple point at Mt. Moosilauke, New Hampshire. Am. Mineral. 67, 1118–1134.
Hoepffner, C., Soulaimani, A., Piqué, A., 2005. The Moroccan Hercynides. J. Afr. Earth Sci. 43, 144–165.
Hoepffner, C., Houari, M.R., Bouabdelli, M., 2006. Tectonics of the North African Variscides (Morocco, western Algeria): an outline. C. R. Geosci. 338, 25–40.
Holland, T., Blundy, J., 1994. Non-ideal interactions in calcic amphiboles and their bearing on amphibole–plagioclase thermometry. Contrib. Mineral. Petrol. 116, 433–447.
Horstwood, M.S., Foster, G.L., Parrish, R.R., Noble, S.R., Nowell, G.M., 2003. Common-Pb corrected in situ U–Pb accessory mineral geochronology by LA-MC-ICP-MS. J. Anal. At. Spectrom. 18, 837–846.
Ilavsky, J., Snopkova, P., 1987. Découverte d'Acritarches paleozoiques dans les terrains métamorphiques de l'Edough (Wilaya d'Annaba, Algérie). C. R. Acad. Sci. Paris Sér. II 305, 881–884.
Irvine, T., Baragar, W., 1971. A guide to the chemical classification of the common volcanic rocks. Canad. J. Earth Sci. 8, 523–548.
Jacobsen, S.B., Wasserburg, G.J., 1980. Sm–Nd isotopic evolution of chrondrites. Earth Planet. Sci. Lett. 50, 139–155.
Johanesen, K., Platt, J.P., Kaplan, M.S., Ianno, A.J., 2014. A revised thermal history of the Ronda peridotite, S. Spain: new evidence for excision during exhumation. Earth Planet. Sci. Lett. 393, 187–199.
Jolivet, L., Augier, R., Faccenna, C., Negro, F., Rimmele, G., Agard, P., Robin, C., Rossetti, F., Crespo-Blanc, A., 2008. Subduction, convergence and the mode of backarc extension in the Mediterranean region. Bull. Soc. Géol. France 179, 525–550.
Jolly, W.T., Lidiak, E.G., Dickin, A.P., 2006. Cretaceous to Mid-Eocene pelagic sediment budget in Puerto Rico and the Virgin Islands (northeast Antilles Island arc). Geol. Acta 4, 35–62.
Jourdan, F., Renne, P.R., 2007. Age calibration of the Fish Canyon sanidine $^{40}Ar/^{39}Ar$ dating standard using primary K–Ar standards. Geochim. Cosmochim. Acta 71, 387–402.
Khedr, M.Z., Arai, S., Python, M., Tamura, A., 2014. Chemical variations of abyssal peridotites in the central Oman ophiolite: evidence of oceanic mantle heterogeneity. Gondwana Res. 25, 1242–1262.
Kretz, R., 1983. Symbols for rock-forming minerals. Am. Mineral. 68, 277–279.
Kroner, U., Romer, R.L., 2013. Two plates—many subduction zones: the Variscan orogeny reconsidered. Gondwana Res. 24, 298–329.
Laouar, R., Boyce, A.J., Ahmed-Said, Y., Ouabadi, A., Fallick, A.E., Toubal, A., 2002. Stable isotope study of the igneous, metamorphic and mineralized rocks of the Edough complex, Annaba, Northeast Algeria. J. Afr. Earth Sci. 35, 271–283.
Leake, B.E., Woolley, A.R., Arps, C.E.S., Birch, W.D., Gilbert, M.C., Grice, J.D., Hawthorne, F.C., Kato, A., Kisch, H.J., Krivovichev, V.G., Linthout, K., Laird, J., Mandarino, J.A., Maresch, W.V., Nickel, E.H., Rock, N.M.S., Schumacher, J.C., Smith, D.C., Stephenson, N.C.N., Ungaretti, L., Whittaker, E.J.W., Youzhi, G., 1997. Nomenclature of amphiboles: report of the Subcommittee on Amphiboles of the International Mineralogical Association, Commission on New Minerals and Mineral Names. Am. Mineral. 82, 1019–1037.
Lebas, M.J., Le Maitre, R.W., Streckeisen, A., Zanettin, B., 1986. A chemical classification of volcanic rocks based on the total alkali-silica diagram. J. Petrol. 27, 745–750.
Le Fèvre, B., (Ph.D. thesis) 2002. Développements chimiques et instrumentaux en géochimie, en vue des analyses isotopiques Lu–Hf et Sm–Nd. Applications à la géochronologie des roches métamorphiques de haut degré. University of Clermont Ferrand, pp. 253.
Linnemann, U., McNaughton, N.J., Romer, R.L., Gehmlich, M., Drost, K., Tonk, C., 2004. West African provenance for Saxo-Thuringia (Bohemian Massif): did Armorica ever leave pre-Pangean Gondwana? U/Pb SHRIMP zircon evidence and the Nd isotopic record. Int. J. Earth Sci. 93, 683–705.
Linnemann, U., Pereira, F., Jeffries, T.E., Drost, K., Gerdes, A., 2008. The Cadomian Orogeny and the opening of the Rheic Ocean: the diacrony of geotectonic processes constrained by LA-ICP-MS U–Pb zircon dating (Ossa-Morena and Saxo-Thuringian Zones, Iberian and Bohemian Massifs). Tectonophysics 461, 21–43.
Linnemann, U., Ouzegane, K., Drareni, A., Hofmann, M., Becker, S., Gärtner, A., Sagawe, A., 2011. Sands of West Gondwana: an archive of secular magmatism and plate interactions — a case study from the Cambro-Ordovician section of the Tassili Ouan Ahaggar (Algerian Sahara) using U–Pb LA-ICP-MS detrital zircon ages. Lithos 123, 188–203.
Lonergan, L., Platt, J.P., 1995. The Malaguide-Alpujarride boundary: a major extensional contact in the Internal Zone of the eastern Betic Cordillera, SE Spain. J. Struct. Geol. 17, 1655–1671.
Lonergan, L., White, N., 1997. Origin of the Betic-Rif mountain belt. Tectonics 16, 504–522.
Ludwig, K.R., 2002. Using Isoplot/Ex. A Geochronological Toolkit for Microsoft Excel. Berkeley Geochronology Center, Special Publication, pp. 1.
Marchesi, C., Garrido, C.J., Bosch, D., Bodinier, J.L., Hidas, K., Padrón-Navarta, J.A., Gervilla, F., 2012. A Late Oligocene suprasubduction setting in the Westernmost Mediterranean revealed by intrusive pyroxenite dikes in the Ronda peridotite (Southern Spain). J. Geol. 120, 237–247.
Maury, R.C., Fourcade, S., Coulon, C., El Azzouzi, M., Bellon, H., Coutelle, A., Ouabadi, A., Semroud, B., Megartsi, M., Cotton, J., Belanteur, O., Hacini, A.L., Piqué, A., Capdevila, R., Hernandez, J., Rehault, J.P., 2000. Post-collisional Neogene magmatism of the Mediterranean Maghreb margin: a consequence of slab breakoff. C. R. Acad. Sci. Paris Sér. II 331, 159–173.
McLennan, S.M., 2001. Relationships between the trace element composition of sedimentary rocks and upper continental crust. Geochem. Geophys. Geosyst. 2, 2000GC000109.
Medaouri, M., Déverchère, J., Graindorge, D., Bracene, R., Badji, R., Ouabadi, A., Yelles-Chaouche, K., Bendiab, F., 2014. The transition from Alboran to Algerian basins (Western Mediterranean Sea): chronostratigraphy, deep crustal structure and tectonic evolution at the rear of a narrow slab rollback system. J. Geodyn. 77, 186–205.
Menegon, L., Pennacchioni, G., Stünitz, H., 2006. Nucleation and growth of myrmekite during ductile shear deformation in metagranites. J. Metamorph. Geol. 24, 553–568.
Menegon, L., Fusseis, F., Stünitz, H., Xiao, X., 2015. Creep cavitation bands control porosity and fluid flow in lower crustal shear zones. Geology 43, 227–230.
Michard, A., Negro, F., Saddiqi, O., Bouybaouene, M.L., Chalouan, A., Montigny, R., Goffé, B., 2006. Pressure–temperature–time constraints on the Maghrebide mountain building: evidence from the Rif–Betic transect (Morocco, Spain), Algerian correlations, and geodynamic implications. C. R. Geosci. 338, 92–114.
Michard, A., Soulaimani, A., Hœpffner, C., Ouanaimi, H., Baidder, L., Rjimati, E.C., Saddiqi, O., 2010. The south-western branch of the Variscan Belt: evidence from Morocco. Tectonophysics 492, 1–24.
Miller, D.M., Goldstein, S.L., Langmuir, C.H., 1994. Ce/Pb and Pb isotope ratios in arc magmas and the enrichment of lead in the continents. Nature 368, 514–520.
Millot, R., Allègre, C.J., Gaillardet, J., Roy, S., 2004. Lead isotopic systematics of major river sediments: a new estimate of the Pb isotopic composition of the Upper Continental Crust. Chem. Geol. 203, 75–90.
Monié, P., Montigny, R., Maluski, H., 1992. Ages $^{40}Ar/^{39}Ar$ alpins de la tectonique ductile extensive dans le massif de l'Edough (Kabylies, Algérie). Bull. Soc. Géol. France 163, 571–584.
Monié, P., Torres-Roldán, R.L., García-Casco, A., 1994. Cooling and exhumation of the western Betic Cordilleras, $^{40}Ar/^{39}Ar$ thermochronological constraints on a collapsed terrane. Tectonophysics 238, 353–379.
Müntener, O., Hermann, J., Trommsdorff, V., 2000. Cooling history and exhumation of lower-crustal granulite and upper mantle (Malenco, Eastern Central Alps). J. Petrol. 41, 175–200.
Obata, M., 1980. The Ronda peridotite: garnet, spinel, and plagioclase lherzolite facies and the P–T trajectories of a high-temperature mantle intrusion. J. Petrol. 21, 533–572.

Oliver, N.H.S., Valenta, R.K., Wall, V.J., 1990. The effect of heterogeneous stress and strain on metamorphic fluid flow, Mary Kathleen, Australia, and a model for large-scale fluid circulation. J. Metamorph. Geol. 8, 311–331.
Paquette, J.L., Ménot, R.P., Pin, C., Orsini, J.B., 2003. Episodic and short-lived granitic pulses in a post-collisional setting: evidence from precise U–Pb zircon dating through a crustal cross-section in Corsica. Chem. Geol. 198, 1–20.
Pearce, J.A., Peate, D.W., 1995. Tectonic implications of the composition of volcanic arc magmas. Annu. Rev. Earth Planet. Sci. 23, 251–286.
Pearce, T.H., Gorman, B.E., Birkett, T.C., 1975. The TiO_2–K_2O–P_2O_5 diagram: a method of discriminating between oceanic and non-oceanic basalts. Earth Planet. Sci. Lett. 24, 419–426.
Pearce, N.J., Perkins, W.T., Westgate, J.A., Gorton, M.P., Jackson, S.E., Neal, C.R., Chenery, S.P., 1997. A compilation of new and published major and trace element data for NIST SRM 610 and NIST SRM 612 glass reference materials. Geostand. Newslett. 21, 115–144.
Peucat, J.J., Mahdjoub, Y., Drareni, A., 1996. U Pb and Rb Sr geochronological evidence for late Hercynian tectonic and Alpine overthrusting in Kabylian metamorphic basement massifs (northeastern Algeria). Tectonophysics 258, 195–213.
Pin, C., Telouk, P., Imbert, J.L., 1995. Direct determination of the samarium: neodymium ratio in geological materials by inductively coupled plasma quadrupole mass spectrometry with cryogenic desolvation. Comparison with isotope dilution thermal ionization mass spectrometry. J. Anal. At. Spectrom. 10, 93–98.
Plank, T., Langmuir, C.H., 1998. The chemical composition of subducting sediment and its consequences for the crust and mantle. Chem. Geol. 145, 325–394.
Platt, J.P., Whitehouse, M.J., 1999. Early Miocene high-temperature metamorphism and rapid exhumation in the Betic Cordillera (Spain): evidence from U–Pb zircon ages. Earth Planet. Sci. Lett. 171, 591–605.
Pryer, L.L., 1993. Microstructures in feldspars from a major crustal thrust zone: the Grenville Front, Ontario, Canada. J. Struct. Geol. 15, 21–36.
Puga, E., Fanning, M., de Federico, A.D., Nieto, J.M., Beccaluva, L., Bianchini, G., Puga, M.A.D., 2011. Petrology, geochemistry and U–Pb geochronology of the Betic Ophiolites: inferences for Pangaea break-up and birth of the westernmost Tethys Ocean. Lithos 124, 255–272.
Roddick, J.C., Cliff, R.A., Rex, D.C., 1980. The evolution of excess argon in alpine biotites $^{40}Ar/^{39}Ar$ analysis. Earth Planet. Sci. Lett. 48, 185–208.
Romagny, A., Munch, P., Cornee, J.J., Corsini, M., Azdimousa, A., Melinte-Dobrinescu, M.C., Drinia, H., Bonno, M., Arnaud, N., Monié, P., 2014. Late Miocene to present-day exhumation and uplift of the Internal Zone of the Rif chain: insights from low temperature thermochronometry and basin analysis. J. Geodyn. 77, 39–55.
Roser, B.P., Korsch, R.J., 1988. Provenance signatures of sandstone-mudstone suites determined using discriminant function analysis of major-element data. Chem. Geol. 67, 119–139.
Rossetti, F., Theye, T., Lucci, F., Bouybaouene, M.L., Dini, A., Gerdes, A., Phillips, D., Cozzupoli, D., 2010. Timing and modes of granite magmatism in the core of the Alboran Domain, Rif chain, northern Morocco: implications for the Alpine evolution of the western Mediterranean. Tectonics 29, TC2017, http://dx.doi.org/10.1029/2009TC002487.
Rossi, P., Cocherie, A., Fanning, C.M., Deloule, E., 2006. Variscan to eo-Alpine events recorded in European lower-crust zircons sampled from the French Massif Central and Corsica, France. Lithos 87, 235–260.
Royden, L.H., 1993. Evolution of retreating subduction boundaries formed during continental collision. Tectonics 12, 629–638.
Rudnick, R.L., Goldstein, S.L., 1990. The Pb isotopic compositions of lower crustal xenoliths and the evolution of lower crustal Pb. Earth Planet. Sci. Lett. 98, 192–207.
Ruiz-Cruz, M.D., De Galdeano, C.S., 2012. Diamond and coesite in ultrahigh-pressure–ultrahigh-temperature granulites from Ceuta, Northern Rif, northwest Africa. Mineral. Mag. 76, 683–705.
Schaltegger, U., Brack, P., 2007. Crustal-scale magmatic systems during intracontinental strike-slip tectonics: U–Pb and Hf isotopic constraints from Permian magmatic rocks of the Southern Alps. Int. J. Earth Sci. 96, 1131–1151.
Simpson, C., Wintsch, R.P., 1989. Evidence for deformation-induced K-feldspar replacement by myrmekite. J. Metamorph. Geol. 7, 261–275.
Stampfli, G.M., Borel, G.D., 2002. A plate tectonic model for the Paleozoic and Mesozoic constrained by dynamic plate boundaries and restored synthetic oceanic isochrons. Earth Planet. Sci. Lett. 196, 17–33.
Steiger, R., Jäger, E., 1977. Subcommission on geochronology: convention on the use of decay constants in geo-and cosmochronology. Earth Planet. Sci. Lett. 36, 359–362.
Sun, S.S., McDonough, W.F., 1989. Chemical and isotopic systematics of oceanic basalts: implications for mantle composition and processes. Geol. Soc. Lond., Spec. Publ. 42, 313–345.
Taylor, S.R., McLennan, S.M., McCulloch, M.T., 1983. Geochemistry of loess, continental crustal composition and crustal model ages. Geochim. Cosmochim. Acta 47, 1897–1905.
Taylor, S.R., McLennan, S.M., 1985. The Continental Crust: Its Composition and Evolution. Blackwell, pp. 312.
Tribuzio, R., Thirlwall, M.F., Messiga, B., 1999. Petrology, mineral and isotope geochemistry of the Sondalo gabbroic complex (Central Alps, Northern Italy): implications for the origin of post-Variscan magmatism. Contrib. Mineral. Petrol. 136, 48–62.
Van Achterberg, E., Ryan, C.G., Jackson, S.E., Griffin, W., 2001. Data reduction software for LA-ICP-MS. In: Sylvester, P. (Ed.), Laser Ablation ICP-MS in the Earth Science, vol. 29. Mineralogical Association of Canada, pp. 239–243.
Vervoort, J.D., Patchett, P.J., 1996. Behavior of hafnium and neodymium isotopes in the crust: constraints from Precambrian crustally derived granites. Geochim. Cosmochim. Acta 60, 3717–3733.
Vervoort, J.D., Patchett, P.J., Albarède, F., Blichert-Toft, J., Rudnick, R., Downes, H., 2000. Hf–Nd isotopic evolution of the lower crust. Earth Planet. Sci. Lett. 181, 115–129.
Vervoort, J.D., Plank, T., Prytulak, J., 2011. The Hf–Nd isotopic composition of marine sediments. Geochim. Cosmochim. Acta 75, 5903–5926.
Villa, I.M., 1998. Isotopic closure. Terra Nova 10, 42–47.
Weill, D.F., Drake, M.J., 1973. Europium anomaly in plagioclase feldspar: experimental results and semiquantitative model. Science 180, 1059–1060.
Wiedenbeck, M., Alle, P., Corfu, F., Griffin, W.L., Meier, M., Oberli, F., Vonquadt, A., Roddick, J.C., Spiegel, W., 1995. Three natural zircon standards for U–Th–Pb, Lu–Hf, trace element and REE analyses. Geostand. Newslett. 19, 1–23.
Workman, R.K., Hart, S.R., 2005. Major and trace element composition of the depleted MORB mantle (DMM). Earth Planet. Sci. Lett. 231, 53–72.
Zeck, H.P., Monié, P., Villa, I.M., Hansen, B.T., 1992. Very high rates of cooling and uplift in the Alpine belt of the Betic Cordilleras, southern Spain. Geology 20, 79–82.
Zheng, Y.F., Gao, X.Y., Chen, R.X., Gao, T., 2011. Zr-in-rutile thermometry of eclogite in the Dabie orogen: constraints on rutile growth during continental subduction-zone metamorphism. J. Asian Earth Sci. 40, 427–451.
Zindler, A., Staudigel, H., Hart, S.R., Endres, R., Goldstein, S., 1983. Nd and Sm isotopic study of a mafic layer from Ronda ultramafic complex. Nature 304, 226–228.
Zindler, A., Hart, S., 1986. Chemical geodynamics. Annu. Rev. Earth Planet. Sci. 14, 493–571.